

Investigation of the effects of heteroatom doping on von-Alpen-type NASICON electrolytes and its applications to solid-state sodium batteries

Gunhee Park^{1,2,†}, Dong Won Jeon^{3,4,†}, Il-Seop Jang^{1,2}, Byeong-Jun Ahn^{1,2}, Kisang Baek^{1,2}, Bo-Ye Song¹, Eun-hye Kim^{1,2}, Junho Bang^{1,2}, Yun Chan Kang^{2,✉}, Sung Beom Cho^{3,4,✉}, Jinyoung Chun^{1,✉}

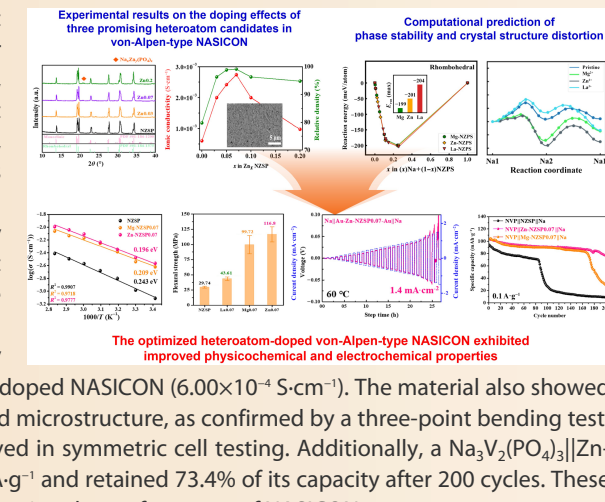
 Cite this article: Park G, Jeon DW, Jang I-S, et al. *J Adv Ceram* 2025, **14**(9): 9221138. <https://doi.org/10.26599/JAC.2025.9221138>

ABSTRACT: The development of electrolytes with high ionic conductivity and stable electrode–electrolyte interfaces is crucial for the practical realization of solid-state sodium batteries. In this study, the effect of heteroatom doping in a von-Alpen-type Na super ionic conductor (NASICON) was investigated by substituting Zr⁴⁺ with Mg²⁺, Zn²⁺, and La³⁺ to enhance its material properties and evaluate its potential for solid-state sodium battery applications. Computational chemistry was employed to predict the thermodynamic stability influenced by dopant introduction and the changes in ionic conductivity arising from crystal structure distortion, with the predictions validated by experiments. The optimized Zn²⁺-doped NASICON (Zn-NZSP0.07) exhibited the highest total ionic conductivity of 2.74×10^{-3} S·cm⁻¹, representing a 4.5-fold increase compared with undoped NASICON (6.00×10^{-4} S·cm⁻¹). The material also showed a high relative density of 99.1%, indicating a compact and well-sintered microstructure, as confirmed by a three-point bending test. Furthermore, a high critical current density of 1.4 mA·cm⁻² was achieved in symmetric cell testing. Additionally, a Na₃V₂(PO₄)₃||Zn-NZSP0.07||Na cell delivered an initial capacity of 103.9 mAh·g⁻¹ at 0.1 A·g⁻¹ and retained 73.4% of its capacity after 200 cycles. These results demonstrate that optimal heteroatom doping is crucial for enhancing the performance of NASICON.

KEYWORDS: Na super ionic conductor (NASICON); solid-state sodium metal battery; heteroatom-doping; computational chemistry; solid-state reaction

1 Introduction

Lithium-ion batteries (LIBs) are widely used in various electronic devices, electric vehicles, and large-scale energy storage systems, with demand continuing to rise [1–5]. However, lithium is heavily concentrated in certain countries, making its price highly volatile [6]. Additionally, the liquid organic electrolytes used in LIBs present issues such as flammability, leakage, and volatility [7]. To address these drawbacks, it is essential to develop more cost-effective and stable batteries. Sodium-ion batteries (SIBs) are a promising alternative to LIBs; they not only share structural similarities with LIBs but also utilize Na⁺, one of the most abundant resources on Earth, which offers potential cost reduction benefits [8–11]. However, safety concerns persist due to the use of liquid organic electrolytes [12]. As a solution, the



The optimized heteroatom-doped von-Alpen-type NASICON exhibited improved physicochemical and electrochemical properties

development of batteries that employ inorganic solid electrolytes as substitutes for liquid organic electrolytes has emerged as an alternative option [13–18]. Among the various candidates for solid electrolytes, oxide-based solid electrolytes exhibit high thermal and chemical stability, as well as a wide electrochemical window, enabling battery operation over a broad temperature range [19–22]. Consequently, significant research is being conducted in this area [23,24]. NASICON (Na super ionic conductor), a representative oxide-based solid electrolyte, has relatively high ionic conductivity ($\sim 10^{-4}$ S·cm⁻¹) compared with other oxide solid electrolytes and remains stable in the presence of moisture, making it suitable for applications in advanced sodium-based battery technologies, including solid-state sodium batteries, hybrid sodium-air batteries, and seawater batteries [25,26].

The NASICON compound was first proposed in 1976 by

† Gunhee Park and Dong Won Jeon contributed equally to this work.

¹Emerging Materials R & D Division, Korea Institute of Ceramic Engineering and Technology (KICET), Jinju 52851, Republic of Korea. ²Department of Materials Science and Engineering, Korea University, Seoul 02841, Republic of Korea. ³Department of Materials Science and Engineering, Ajou University, Suwon 16499, Republic of Korea. ⁴Department of Energy Systems Research, Ajou University, Suwon 16499, Republic of Korea.

✉ Corresponding authors. E-mail: J. Chun, jchun@kicet.re.kr; S. Cho, csb@ajou.ac.kr; Y. Kang, yckang@korea.ac.kr

Received: May 21, 2025; Revised: July 4, 2025; Accepted: July 18, 2025

© The Author(s) 2025. This is an open access article under the terms of the Creative Commons Attribution 4.0 International License (CC BY 4.0, <http://creativecommons.org/licenses/by/4.0/>).

Goodenough *et al.* [27] and Hong [28]. Structurally, this compound forms a three-dimensional framework through the sharing of oxygen atoms between $\text{PO}_4(\text{SiO}_4)$ tetrahedra and ZrO_6 octahedra, represented by the general formula $\text{Na}_{1+x}\text{Zr}_2\text{Si}_x\text{P}_{3-x}\text{O}_{12}$ [29]. Among these, $\text{Na}_3\text{Zr}_2\text{Si}_2\text{PO}_{12}$ ($x = 2$) is a representative compound known for its high ionic conductivity at room temperature and is commonly referred to as Hong-type NASICON (H-NASICON) [30–33]. However, a significant issue with H-NASICON is the formation of a ZrO_2 secondary phase during the high-temperature sintering process. ZrO_2 is a non-conductive phase that can degrade both the ionic conductivity and mechanical strength of NASICON [34–36]. To address this issue, renewed attention has been given to the Zr^{4+} -deficient NASICON composition $\text{Na}_{0.8+x}\text{Zr}_{1.55}\text{Si}_x\text{P}_{3-x}\text{O}_{11}$, as proposed by von Alpen [37,38]. The von-Alpen-type NASICON (vA-NASICON) compound, with the composition $\text{Na}_{3.1}\text{Zr}_{1.55}\text{Si}_{2.3}\text{P}_{0.7}\text{O}_{11}$ ($x = 2.3$), suppresses the formation of ZrO_2 secondary phases due to its inherently lower Zr^{4+} content than H-NASICON, achieving an ionic conductivity of $9.00 \times 10^{-4} \text{ S}\cdot\text{cm}^{-1}$ and enhanced mechanical strength [26]. Most of the previously reported NASICON literatures were based on the H-NASICON composition, and research about utilizing the vA-NASICON composition is lacking. Therefore, this study employed the vA-NASICON composition to explore various research possibilities.

Although the NASICON compound has a relatively high ionic conductivity compared with other oxide-based solid electrolytes, it remains lower than that of liquid organic electrolytes ($10^{-2} \text{ S}\cdot\text{cm}^{-1}$) [39,40]. One effective method to increase this conductivity is the introduction of heteroatoms, an approach explored in various studies [41]. When heteroatoms are doped into NASICON, the bottleneck size for sodium ions can be expanded depending on the kind of dopant used [42,43]. Substituting dopants with lower oxidation states than Zr^{4+} compensates for the charge balance by increasing the sodium ion concentration, thereby improving the ionic conductivity [44,45]. Therefore, it is crucial to consider the differences in ionic radius and oxidation state relative to Zr^{4+} when introducing heteroatoms, as well as to ensure the thermodynamic stability of the NASICON crystalline phase, and to prevent excessive formation of secondary phases [46,47]. Table S1 in the Electronic Supplementary Material (ESM) presents the results of a comparison of the ionic conductivity and activation energy after H-NASICON was doped with heteroatoms via the solid-state reaction method, which is highly accessible and scalable [41,43,48–54]. In one representative study, Samiee *et al.* [55] achieved a total ionic conductivity of $2.05 \times 10^{-3} \text{ S}\cdot\text{cm}^{-1}$ at room temperature by doping NASICON with Mg^{2+} . Jolley *et al.* [41] reported that substituting Zr^{4+} with divalent cations (Co, Ni, Zn) increased the sodium ion content within the NASICON structure, thereby improving the bulk conductivity. The sample that exhibited the greatest increase in bulk conductivity was the Zn-doped NASICON sample, whose bulk conductivity increased approximately threefold compared with that of the undoped NASICON sample. As a result, the total ionic conductivity of the Zn-doped NASICON reached $8.05 \times 10^{-4} \text{ S}\cdot\text{cm}^{-1}$. Among the divalent dopants, Wang *et al.* [54] introduced Cu^{2+} and reported that the CuO precursor could also act as a sintering aid, reducing the sintering temperature and enhancing the ionic conductivity. Consequently, the optimized Cu-doped NASICON demonstrated an ionic conductivity of $5.57 \times 10^{-4} \text{ S}\cdot\text{cm}^{-1}$ under sintering conditions at 1150°C for 12 h. Finally, Sun *et al.* [56] reported that La^{3+} doping increased the Si/P ratio in the NASICON structure, resulting in changes in the atomic ratio and enhanced Na ion occupancy due to charge imbalance, thus accelerating

ionic movement. Based on various reports on heteroatom doping in H-NASICON, we predicted the behavior of vA-NASICON when it was doped with similar elements. In H-NASICON, Mg^{2+} and Zn^{2+} doping are known to increase the ionic conductivity by increasing the sodium ion concentration in the structure, whereas La^{3+} doping, despite the formation of multiple secondary phases, is expected to contribute to improved ionic transport. Although extensive studies have been conducted on the effect of heteroatom doping in H-NASICON, approaches similar to those used in vA-NASICON remain scarce. Considering these findings, it is crucial to investigate and design effective heteroatom doping strategies tailored to vA-NASICON in order to improve essential properties such as ionic conductivity and density.

In this study, we investigated the aliovalent doping effects of three promising heteroatom candidates that are expected to enhance the main properties of vA-NASICON. When optimal amounts of Mg^{2+} and Zn^{2+} were introduced, both the ionic conductivity and relative density increased, which was accompanied by the observation of a uniform NASICON crystalline phase. In contrast, even a trace amount of La^{3+} led to the formation of a secondary phase, resulting in a deterioration of ionic conductivity and density. The formation of a secondary phase, which is influenced by dopants, is consistent with the results of density functional theory calculations. Additionally, we suggested the effects of introducing Mg^{2+} and Zn^{2+} on the changes in the ion diffusion coefficient and Na^+ transport channel geometry. For the optimized Zn^{2+} -doped vA-NASICON, which exhibited the best performance, a high ionic conductivity of $2.74 \times 10^{-3} \text{ S}\cdot\text{cm}^{-1}$ and a relative density of 99.1% were observed, even at a sintering temperature below 1200°C . Furthermore, the average three-point bending strength was 116.8 MPa, which is four times higher than that of undoped vA-NASICON. These improvements in the main properties resulted in enhanced electrochemical properties, demonstrating a high critical current density of $1.4 \text{ mA}\cdot\text{cm}^{-2}$ and sustaining operation for over 500 h in a symmetric cell. In solid-state sodium cell tests employing a $\text{Na}_3\text{V}_2(\text{PO}_4)_3$ (NVP) cathode and a Na metal anode, excellent capacity retention of approximately 73.4% of the initial capacity was observed after 200 cycles at a current density of $0.1 \text{ A}\cdot\text{g}^{-1}$. This study is highly important because it investigates the property variations induced by the incorporation of various heteroatoms into the vA-NASICON composition and suggests its potential application in solid-state sodium batteries.

2 Experimental

2.1 Materials synthesis

The NASICON compounds with $\text{Na}_{3.1}\text{Zr}_{1.55}\text{Si}_{2.3}\text{P}_{0.7}\text{O}_{11}$ (NZSP), $\text{Na}_{3.1+2x}\text{Zr}_{1.55-x}\text{M}_x\text{Si}_{2.3}\text{P}_{0.7}\text{O}_{11}$ ($\text{M} = \text{Mg}^{2+}, \text{Zn}^{2+}$, M-NZSPx), and $\text{Na}_{3.1+2x}\text{Zr}_{1.55-x}\text{M}'_x\text{Si}_{2.3}\text{P}_{0.7}\text{O}_{11}$ ($\text{M}' = \text{La}^{3+}$, M'-NZSPx) were prepared according to the stoichiometric ratio via a conventional solid-state reaction method (Fig. S1 in the ESM). Precursors, including $\text{Na}_3\text{PO}_4 \cdot 12\text{H}_2\text{O}$ (Sigma-Aldrich, 98.0%), Na_2CO_3 (Sigma-Aldrich, 99.5%), SiO_2 (Junsei Chemical Co., Ltd., 99.5%), ZrO_2 (Samchun Chemicals, 99.0%), MgO (Sigma-Aldrich, 98.0%), ZnO (KANTO Chemical Co., Inc., 99.0%), and La_2O_3 (Samchun chemicals, 99.9%), were uniformly mixed via a planetary ball mill (Fritsch, Pulverizette7 PL) for 4 h. Anhydrous ethanol was used as the solvent. The mixed precursor was then dried at 80°C for over 4 h to evaporate the solvent. The dried powder was subsequently calcined at 1100°C for 10 h. After calcination, the agglomerated granules were crushed again via a planetary ball mill and dried. The powdered material obtained was formed into pellets with $\Phi =$

13 mm using a uniaxial press and sintered at 1180 °C for 12 h in a box furnace. Following the completion of sintering, natural cooling was carried out in air. The resulting pellets were polished to achieve a clean surface using sandpaper with gradually increasing grit from #400 to #2000.

2.2 Microstructure analysis of samples

The crystal structure of the sintered samples was analyzed via an X-ray diffractometer (D8 Advance, Bruker) with Cu K α radiation ($\lambda = 1.5418 \text{ \AA}$), and a diffraction angle range of 10°–40°. Rietveld refinement was performed for lattice structure observation via GSAS-II software. Microstructural observations were conducted via a field-emission scanning electron microscope (FE-SEM; JSM-7610F, JEOL). For elemental mapping of the samples, an energy-dispersive X-ray spectrometer was employed in conjunction with FE-SEM. A Raman spectrometer (532 nm laser, RAMANTouch, Bruker) was used to determine the crystal phase. The mechanical strength of the NASICON ceramics was analyzed via a three-point bending test with a universal testing machine (UTM; AGS-1kNX, SHIMADZU). The test samples were rectangular pellets with widths of 3 cm and thicknesses of 1 mm. To eliminate surface impurities, the samples were polished via an autoglasser/polisher (MetPrepTM PH-4TM, Chinwoo Tech). The prepared samples were subjected to bending by lowering the bending jig at a rate of 1 mm·min⁻¹, and the stress at the point of pellet fracture was measured.

2.3 Computational chemistry calculations

All density functional theory (DFT) calculations were carried out via the Vienna *ab initio* simulation package (VASP) [57]. The calculations employed the projector-augmented wave (PAW) method [58], with the exchange-correlation potential described by the generalized gradient approximation (GGA) via the Perdew-Burke-Ernzerhof (PBE) parametrization [59]. A plane-wave energy cutoff of 520 eV was applied, and structural optimizations were performed until the forces on each atom were reduced below 0.01 eV·Å⁻¹. Brillouin zone sampling was conducted with a *k*-point density of 100 Å⁻³ of the reciprocal cell. To generate doped NZSP structures, the special quasirandom structure (SQS) approach was employed for alloying systems via the mcsqs code from the Alloy Theoretic Automated Toolkit (ATAT) [60]. We performed continuous symmetry measurement (CSM) calculations via the Python code introduced by Jun *et al.* [61].

Ab initio molecular dynamics (AIMD) simulations were performed to investigate Na⁺ behavior. These simulations were conducted within the NVT ensemble, employing a Nose-Hoover thermostat [62]. The monoclinic and rhombohedral NZSP unit cells had lattice parameters of approximately 10 Å or more in each direction, and a Γ -centered 1 × 1 × 1 *k*-point grid was applied. The AIMD simulations were run for 60 ps at 800 K, with a time step of 2 fs. For Na⁺ diffusion analysis, probability density analysis was conducted using the diffusion analyzer module in Pymatgen [63]. Diffusion channel size analysis based on Na-ion trajectories from AIMD simulations was performed using the topological analysis package Zeo⁺⁺ [64]. The Na vacancy migration energy barrier was calculated using the climbing-image nudging elastic band (NEB) method. The forces were converged to within 0.05 eV·Å⁻¹. The two Na vacancies were introduced to calculate the Na vacancy migration energy for the Na1-Na2-Na1 path for each pristine and doped case. To compensate for the electrons due to vacancies, the excess electrons were compensated by a uniform background charge. The atomic structures and Na pathway figures were visualized by VESTA [65].

2.4 Electrochemical measurement

The ionic conductivity of the pellets was measured via an electrochemical impedance spectrometer (SP-300, Biologic), with a frequency range from 1 Hz to 7 MHz. The thickness of the samples was adjusted to 1.0–1.1 mm before measurement, and Au electrodes were sputtered on both sides to prevent surface ion blocking. The temperature-dependent ion conductivity was analyzed within the temperature range of 293–353 K. The ionic conductivity (σ) is exponentially dependent on the temperature given by the Arrhenius equation (Eq. (1)):

$$\sigma = \sigma_0 \exp(-E_a/(kT)) \quad (1)$$

where E_a is the activation energy; k is the Boltzmann constant; T is the absolute temperature; σ_0 is a preexponential factor. Cyclic voltammetry (CV) was conducted in the range from -1.0 to 5.0 V using Na||electrolyte||stainless steel cells. The electronic conductivity was calculated through direct current (DC) polarization analysis. The electronic resistance can be calculated based on steady-state current and an applied external voltage of 6 V. The ionic and electronic conductivities (σ_i and σ_e) of NASICON were calculated using Eqs. (2) and (3), respectively:

$$\sigma_i = L/(R \cdot S) \quad (2)$$

$$\sigma_e = I \cdot L/(V \cdot S) \quad (3)$$

where R represents the resistance; L represents the sample thickness; S represents the pellet area; I represents the steady-state current; V represents the external voltage.

The critical current density (CCD) was obtained through experiments with Na||Au-electrolyte-Au||Na symmetric cells. To decrease the contact resistance between the electrolytes and the Na metal electrode, an Au coating was applied to both sides of the sample to form an interlayer. Symmetric cells were assembled in an argon atmosphere glovebox with O₂/H₂O levels below 0.1 ppm. After cell assembly, aging was carried out at 85 °C for 3 h in an oven to improve interfacial contact. The interfacial resistance between the sodium metal and the NASICON electrolyte was subsequently measured before the symmetric cell test, followed by charging/discharging under isothermal conditions at 60 °C.

The preparation of the Na⁺-based cathode involved mixing commercial Na₃V₂(PO₄)₃ (NVP/theoretical capacity: 117 mAh·g⁻¹) powder, Super P, and polyvinylidene fluoride (PVDF) in a weight ratio of 8 : 1 : 1, with N-methyl-2-pyrrolidone (NMP) as the solvent. The resulting slurry was cast with an Al foil with a thickness of 100 μm and dried overnight at 80 °C in a vacuum oven. The loading mass of NVP was ~1.5 mg·cm⁻². During the assembly of the NVP||NASICON||Na metal cell, 5 μL of 1 M NaClO₄ EC/DEC (1 : 1) liquid electrolyte was dropped onto the surface of the cathode. A NASICON pellet was then placed on top, followed by the attachment of a Na metal anode. For internal packing, a spacer with a thickness of 1 mm and a spring were added. The cell was subsequently sealed via a manual crimping machine and charged/discharged in the voltage range of 2.2–3.8 V (vs. Na/Na⁺) at room temperature.

3 Results and discussion

In this study, we selected Mg²⁺, Zn²⁺, and La³⁺ as candidate dopants for vA-NASICON. Compared with Zr⁴⁺, the low valences of Mg²⁺, Zn²⁺, and La³⁺ can increase the concentration of Na⁺ ions added to balance the oxidation number during the doping process, thereby increasing the conductivity of sodium ions. In addition, Mg²⁺

(0.72 Å) and Zn²⁺ (0.74 Å) have ionic radii similar to that of Zr⁴⁺ (0.72 Å), enabling them to preserve the NASICON structure [66]. Although the ionic radius (1.03 Å) of La³⁺ differs significantly, several previous studies have demonstrated that there is a substantial increase in the ionic conductivity of H-NASICON resulting from anomalous behaviors associated with a secondary phase [67,68]. Therefore, we also investigated the effect of introducing La³⁺ on the production of vA-NASICON. Figures 1(a)-1(c) show the X-ray diffraction (XRD) patterns of the NASICON samples doped with various heteroatoms. The undoped NZSP has a monoclinic peak, which corresponds to its most stable phase at room temperature [69]. The XRD patterns of NASICON doped with Mg²⁺ and Zn²⁺ indicate that as the concentration of the heteroatoms increases, the diffraction peak at approximately 19.5° shifts to a lower angle (Fig. S2 in the ESM) [70]. This observation suggests a partial phase transition from the monoclinic phase to the rhombohedral phase as a result of doping. Importantly, within the doping range of 0–0.07 ratio, no impurity diffraction peaks associated with the heteroatoms were detected, indicating that the dopants were incorporated by substituting Zr⁴⁺ sites within the NASICON structure. However, as the doping concentration increases above 0.1, the peak at 21° also increases, which corresponds to the phases bonded with Na, P, and heteroatoms observed as Na_xMg_y(PO₄)_z and Na_xZn_y(PO₄)_z [47,52,71,72]. In contrast, the XRD patterns of the samples doped with La³⁺ tend to differ from those of the samples doped with the other two elements. Even at a low doping ratio of 0.05, a secondary phase composed of Na_xLa_y(PO₄)_z is observed, becoming more prominent as the doping concentration increases (Fig. S3 in the ESM) [68]. La³⁺ tends not to be incorporated into the NASICON structure regardless of the doping concentration, but instead tends to associate with secondary phases such as Na₃PO₄. Moreover, as the La³⁺ doping concentration increases, additional impurity phases, such as La₂O₃, are formed, leading to structural instability. These secondary phases are predominantly located along the grain boundaries [73]. These phases introduce

significant resistance to ion conduction, thereby deteriorating the overall conductivity. Since La³⁺ has poor solubility in our experiments, secondary phases are formed even at a 0.05 doping ratio of La³⁺ and show a proportional pattern as the doping ratio increases. This will be discussed in more detail in a later section with simulation results.

Figures 1(d)–1(f) present the results of the Rietveld refinement analysis based on the XRD diffraction data of the representative samples. The reliability of the analysis was verified through the Chi-square (χ^2) value, with a low χ^2 value of approximately 2%, demonstrating the high reliability of the Rietveld refinement method. Table 1 lists the unit cell volumes, phase fractions, and lattice parameters, with all the samples exhibiting the C2/c space group for their crystal structures. Compared with those of NZSP, the lattice parameters (a , b , c) and unit cell volume of the heteroatom-doped samples (Mg-NZSP0.07 and Zn-NZSP0.07) slightly differ. This is attributed to the incorporation of heteroatoms, which weakens the bonding strength of the oxygen ions relative to that of Zr⁴⁺, thereby inducing structural distortions. In this process, the a - and b -axes tend to increase slightly, whereas the c -axis decreases. These changes suggest a phase transition from a monoclinic to a rhombohedral structure [74]. These structural changes lead to an overall increase in the unit cell volume of heteroatom-doped NZSP compared with undoped NZSP. Consequently, the distortion of the NASICON framework induced by the optimized incorporation of heteroatoms facilitates Na diffusivity.

To support the increase in the proportion of the rhombohedral phase due to the introduction of heteroatoms, Raman spectroscopy was performed. It has been reported that monoclinic NASICON exhibits separated peaks in the range of 950–1030 cm⁻¹, whereas rhombohedral NASICON shows a single peak at 920 cm⁻¹ [70,75]. As observed in Fig. S4(a) in the ESM, NASICON doped with Mg²⁺ and Zn²⁺ exhibited an increased peak at 920 cm⁻¹, which corresponds to the rhombohedral phase, compared with undoped NZSP. Peak deconvolution in the high-

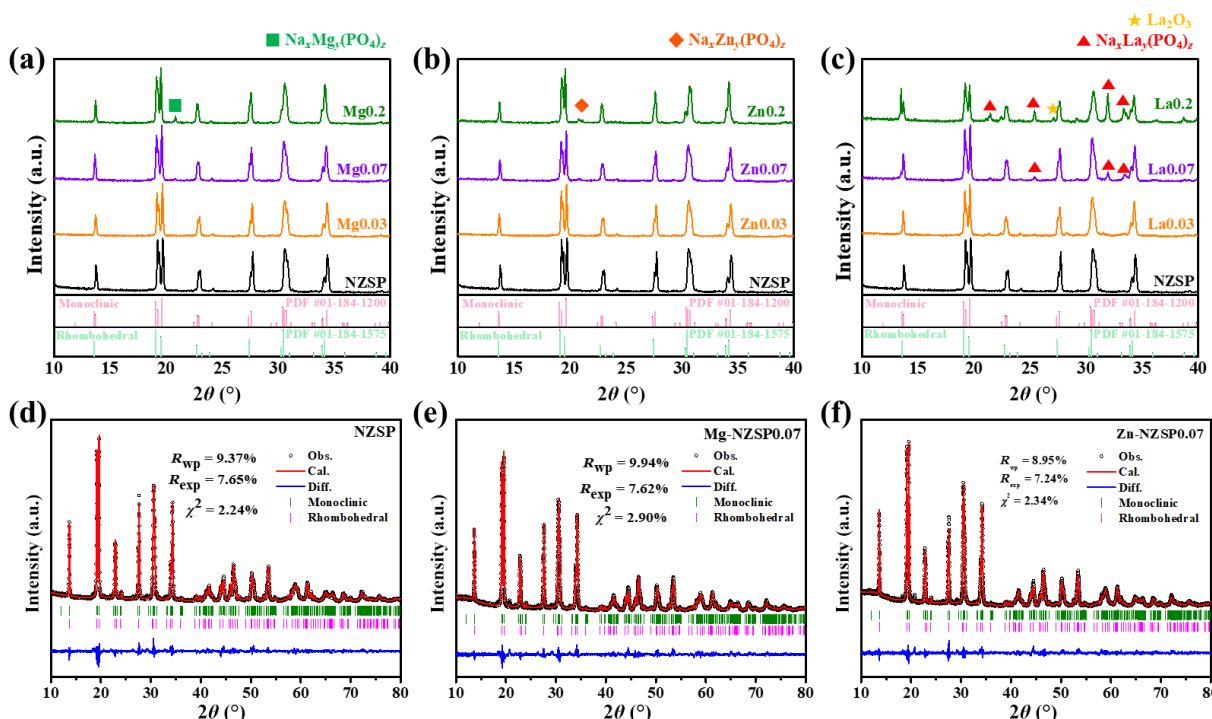


Fig. 1 XRD patterns of (a) Mg-NZSP_x ($x = 0\text{--}0.2$), (b) Zn-NZSP_x ($x = 0\text{--}0.2$), and (c) La-NZSP_x ($x = 0\text{--}0.2$). Rietveld refinement plots of (d) NZSP, (e) Mg-NZSP0.07, and (f) Zn-NZSP0.07.

frequency region where the rhombohedral and monoclinic phases coexist revealed that the sample with optimal heteroatom doping presented a broader peak at approximately 920 cm^{-1} than undoped NZSP (Fig. S4(b) in the ESM). This further demonstrates that heteroatom doping increases the proportion of the rhombohedral phase. A comprehensive analysis through XRD, Rietveld refinement, and Raman spectroscopy reveals that Mg^{2+} and Zn^{2+} not only enable impurity-free NASICON formation across various doping concentrations but also facilitate the stabilization of the rhombohedral phase at room temperature. In contrast, La^{3+} forms undesirable secondary phases even at low doping levels. This was validated by demonstrating behavior similar to that of the phase stability analysis results from computational chemistry.

To compare the phase stability of undoped and heteroatom-doped systems, we constructed a phase diagram of NASICON. To consider only the substitution effect of Zr^{4+} with dopants, we substituted the dopants at the same site in each doping case and introduced additional Na^+ near the dopants. As shown in Fig. 2(a), La-NZSP has the highest energy above the hull among both pristine and doped NASICON in the monoclinic and rhombohedral crystal structures. This indicates that incorporating La^{3+} at the Zr^{4+} site results in less stable substitution than other dopants. Additionally, as mentioned above, when the doping concentration exceeds a certain threshold, secondary phases such as Na_3PO_4 can form at interfaces and react with dopants to create additional insulating phases such as $\text{Na}_x\text{M}_y(\text{PO}_4)_z$ ($M = \text{Mg}^{2+}, \text{Zn}^{2+}$, and La^{3+}). To investigate the interface stability, we examined the reaction between NASICON and Na^+ , which can interact during battery cycling. As shown in Figs. 2(b) and 2(c), the interface reaction energies for La-NZSP, which can lead to Na_3PO_4 formation, are $-218\text{ meV}\cdot\text{atom}^{-1}$ for monoclinic NASICON and $-204\text{ meV}\cdot\text{atom}^{-1}$ for rhombohedral NASICON. These values represent the strongest driving force among all the dopants, indicating that La-NZSP is more prone to forming secondary interphases. Therefore, by combining the energy above the hull and the interface reactivity results, we can infer that the solubility limit of La-NZSP is lower than that of Mg-NZSP and Zn-NZSP, which aligns with the experimental results.

Figure 3 shows the cross-sectional images of the samples observed via FE-SEM. In the case of undoped NZSP (Fig. 3(a)),

large and numerous pores are present at the grain boundaries. This resulted from slow grain growth and insufficient densification at a sintering temperature of $1180\text{ }^\circ\text{C}$. These pores not only decrease the mechanical strength of ceramics but also promote the formation of dendrites from the Na metal anode. In contrast, the cross-sectional images of Mg-NZSP0.07 and Zn-NZSP0.07 reveal more closely packed particles than those of the undoped samples do, indicating improved densification (Figs. 3(b) and 3(c)). The densification of Mg^{2+} -doped NASICON can be attributed to the addition of MgO as a precursor, which enhances the densification rate and surface diffusion coefficient, thereby promoting grain growth [72,76,77]. A similar phenomenon can also occur in Zn^{2+} -doped NASICON. The addition of ZnO as a precursor facilitates the formation of a Zn -rich liquid phase during the sintering process, which enhances mass transport, promotes densification, and accelerates grain growth. These microstructural changes enhance the ionic conductivity [78,79]. As a result, both Mg-NZSP0.07 and Zn-NZSP0.07 not only show slight changes in their crystalline structures and lattice parameters due to the substitution of Zr^{4+} but also exhibit compact microstructures with minimal porosity. However, La-NZSP0.07 has more grain boundaries and a more porous structure than both Mg-NZSP0.07 and Zn-NZSP0.07 do (Fig. 3(d)). Although a previous study reported that La^{3+} can act as an effective sintering aid [50], our results indicate that La_2O_3 is not an effective precursor for achieving a dense microstructure of vA-NZSP under the sintering conditions used in this study. The back-scattered electron (BSE) images, depending on the doping concentration, are presented in Fig. S6 in the ESM. As the doping concentration increased, the porosity of Mg-NZSP x (Fig. S5(b) in the ESM) and Zn-NZSP x (Fig. S5(c) in the ESM) decreased up to an optimal ratio. However, when the doping ratio exceeds 0.1, excessive grain growth occurs, leading to the formation of pores at the grain boundaries. In the case of La-NZSP x , numerous pores were observed regardless of the doping concentration, and no bulk grain growth was detected (Fig. S5(d) in the ESM). These results further indicate that La^{3+} is not a suitable heteroatom for enhancing the main properties of vA-NASICON under the sintering conditions employed in this study.

The element distributions of the samples doped with

Table 1 Lattice parameters and phase fractions of undoped NZSP and optimized heteroatom-doped NZSP

Composition	Space group	Lattice volume (\AA^3)	Crystalline phase fraction (%)		Lattice parameter			
			Monoclinic NASICON	Rhombohedral NASICON	a (\AA)	b (\AA)	c (\AA)	β ($^\circ$)
NZSP	C2/c	1086.307	88.2	11.8	15.676	9.068	9.213	123.96
Mg-NZSP0.07	C2/c	1086.452	81.1	18.9	15.683	9.071	9.212	124.01
Zn-NZSP0.07	C2/c	1086.843	75.6	24.4	15.689	9.072	9.210	124.00

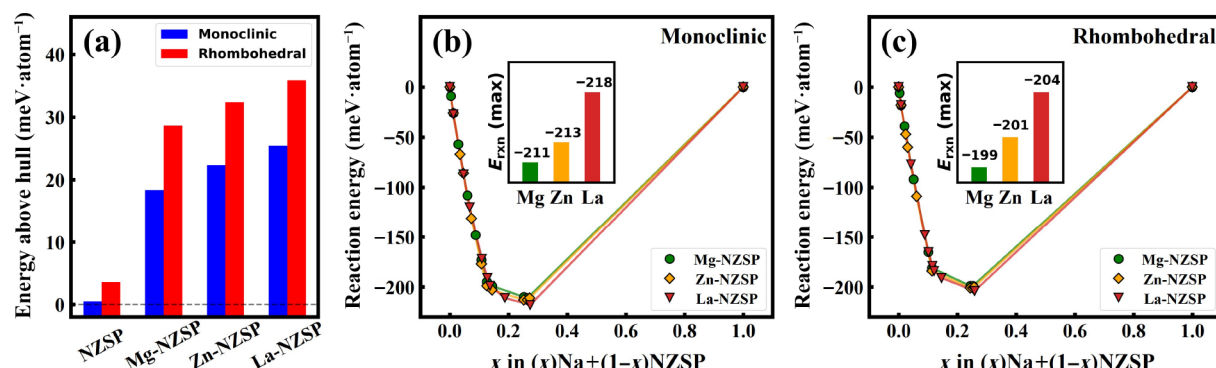


Fig. 2 (a) Energy above hull plots of undoped and heteroatom-doped NASICON. Interface reaction energy plots of (b) monoclinic and (c) rhombohedral NZSP.

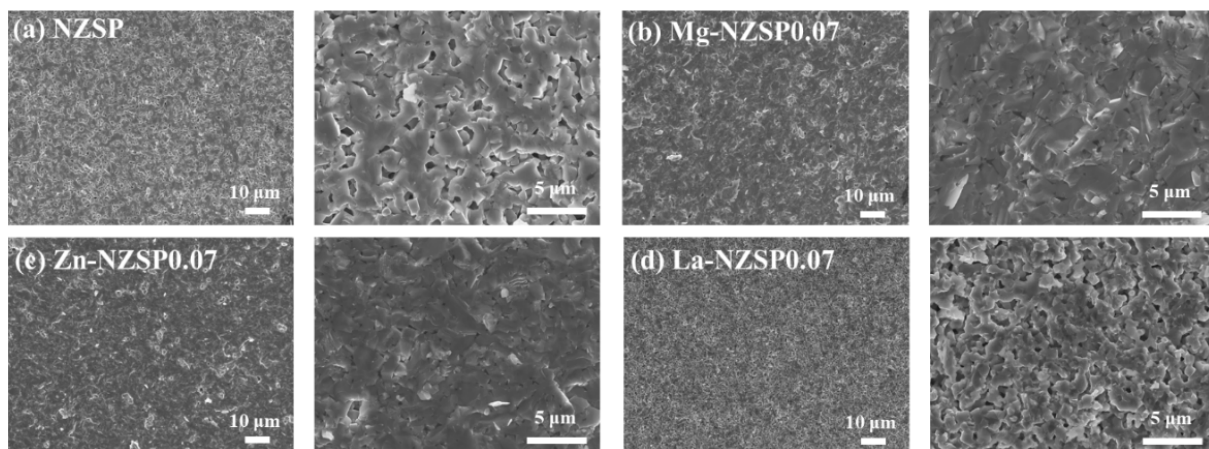


Fig. 3 Cross-section images of NASICON via FE-SEM: (a) NZSP, (b) Mg-NZSP0.07, (c) Zn-NZSP0.07, and (d) La-NZSP0.07.

heteroatoms at a ratio of 0.07 were confirmed by EDS mapping (Fig. 4). Mg^{2+} and Zn^{2+} were uniformly distributed throughout Mg-NZSP0.07 (Fig. 4(b)) and Zn-NZSP0.07 (Fig. 4(c)), respectively. It seems that La^{3+} is also uniformly distributed in La-NZSP0.07 (Fig. 4(d)). However, many white spots observed as intensity differences in BSE images can be identified as secondary phases containing La^{3+} [26,33]. Despite the low dopant concentration, La-NZSP0.07 tended to form secondary or impurity phases rather than being incorporated into the NASICON structure. This observation is also consistent with computational chemistry predictions.

Figures 4(e)–4(g) show the elemental distributions of samples doped with heteroatoms at a ratio of 0.2. The distributions of Mg^{2+} and Zn^{2+} overlapped with those of Na and P, but were opposite to those of Zr and Si, supporting the formation of numerous secondary phases in Mg-NZSP0.2 (Fig. 4(e)) and Zn-NZSP0.2 (Fig. 4(f)). As previously mentioned, excessive doping of heteroatoms combines with Na_3PO_4 , which can also be confirmed in BSE images and is consistent with previously reported results [47]. These secondary phases, comprising heteroatoms and Na and P, form at the grain boundaries and hinder Na^+ ion migration, causing a decrease in ionic conductivity and density. In contrast, La-NZSP0.2 does not show an exact overlap of the La^{3+} signal with Na and P, but it exhibits behavior similar to that of La-NZSP0.07 (Fig. 4(g)). However, when the XRD patterns and BSE images are considered together, this distribution of La^{3+} does not indicate uniform incorporation into the NASICON structure. Instead, this suggests that secondary phases are dispersed throughout La-NZSP0.2. Under the sintering conditions of this study, the formation of these secondary phases significantly decreases the key properties of materials, which will be discussed in the following sections.

Topological analysis was also performed to analyze the effects of structural changes in the Na^+ channel caused by heteroatom substitution on ionic conductivity. As shown in Fig. 5(a), NZSP consists of a framework of non-Na cation polyhedral and Na^+ channels that facilitate ion transport between the frameworks. Na^+ channels are primarily composed of Na-O polyhedra, where Na^+ can occupy tetrahedral and octahedral sites. Jun *et al.* [61] demonstrated that in lithium-ion solid-state electrolytes with a corner-sharing cation framework, the fast diffusion of lithium is facilitated by an increase in distorted lithium-site environments. Consequently, to assess the relationship between Na^+ site distortion and ionic conductivity, we calculated the continuous symmetry measurement (CSM) [80]. A high CSM value indicates that the coordination environment is highly distorted from its

ideal structure. In such a distorted environment, the Na^+ residing at the site becomes less stable and has a higher energy state, reducing the energy barrier for ion migration. Therefore, an appropriate level of distortion can enhance ion mobility, improving the ionic conductivity of NZSP. The CSM values of undoped and heteroatom-doped NZSP are presented in Fig. 5(b). In both the monoclinic and rhombohedral NZSP, upon doping, the CSM peak position of the octahedral sites does not change significantly. However, for the tetrahedral sites, the CSM values partially shift to higher values, whereas the values for La-NZSP remain comparable to those of undoped NZSP. This indicates that when an M^{2+} metal dopant is incorporated into NZSP, the additional Na^+ influences the Na^+ channel, increasing the proportion of highly distorted Na^+ tetrahedral sites, which facilitates Na^+ -ion migration.

The fundamental step in ionic diffusion is the migration of ions between stable sites by overcoming a diffusion barrier [81]. The highest energy along this path corresponds to the migration activation energy, which constitutes the primary component of the activation energy for long-range diffusion in ionic conductors. To analyze the effect of heteroatomic doping on Na^+ channel distortion, we calculated the Na^+ migration energy barrier in monoclinic and rhombohedral NZSP via the climbing-image nudged elastic band (NEB) method [81–82]. The Na^+ migration pathway is shown in Fig. 5(a) and Fig. S6 in the ESM. In the monoclinic structure, Na^+ can occupy three types of Wyckoff positions. However, since the bond lengths of Na_1 -O and Na_3 -O are nearly identical, the Na_3 site can be considered equivalent to the Na_1 site [9,43]. Therefore, only two distinct types of Na^+ sites can be considered in both the monoclinic and rhombohedral NZSPs. To isolate the effects of doping, we substituted the same Zr^{4+} site in each doping case, and NEB calculations were performed after full relaxation of the doped structures. The Na^+ migration energy barriers are presented in Fig. 5(c). Among the monoclinic structures, La-NZSP has the highest migration energy barrier. As shown in Fig. S7 in the ESM, the channel size from Na_2 to Na_1 (final state) in monoclinic La-NZSP is substantially different from that in the other undoped and heteroatom-doped monoclinic cases. This is reflected in the sharp decrease in the relative energy from Na_2 to Na_1 . In contrast, when comparing Mg-NZSP and Zn-NZSP, a slightly larger void space is observed around the Na_2 site in Zn-NZSP. This suggests a difference in the bottleneck size of the channel between stable Na^+ sites, which correlates with the variation in the migration energy barrier from Na_2 to Na_1 (final state) between Mg- and Zn-NZSP. Among the rhombohedral structures, undoped NZSP and La-NZSP have

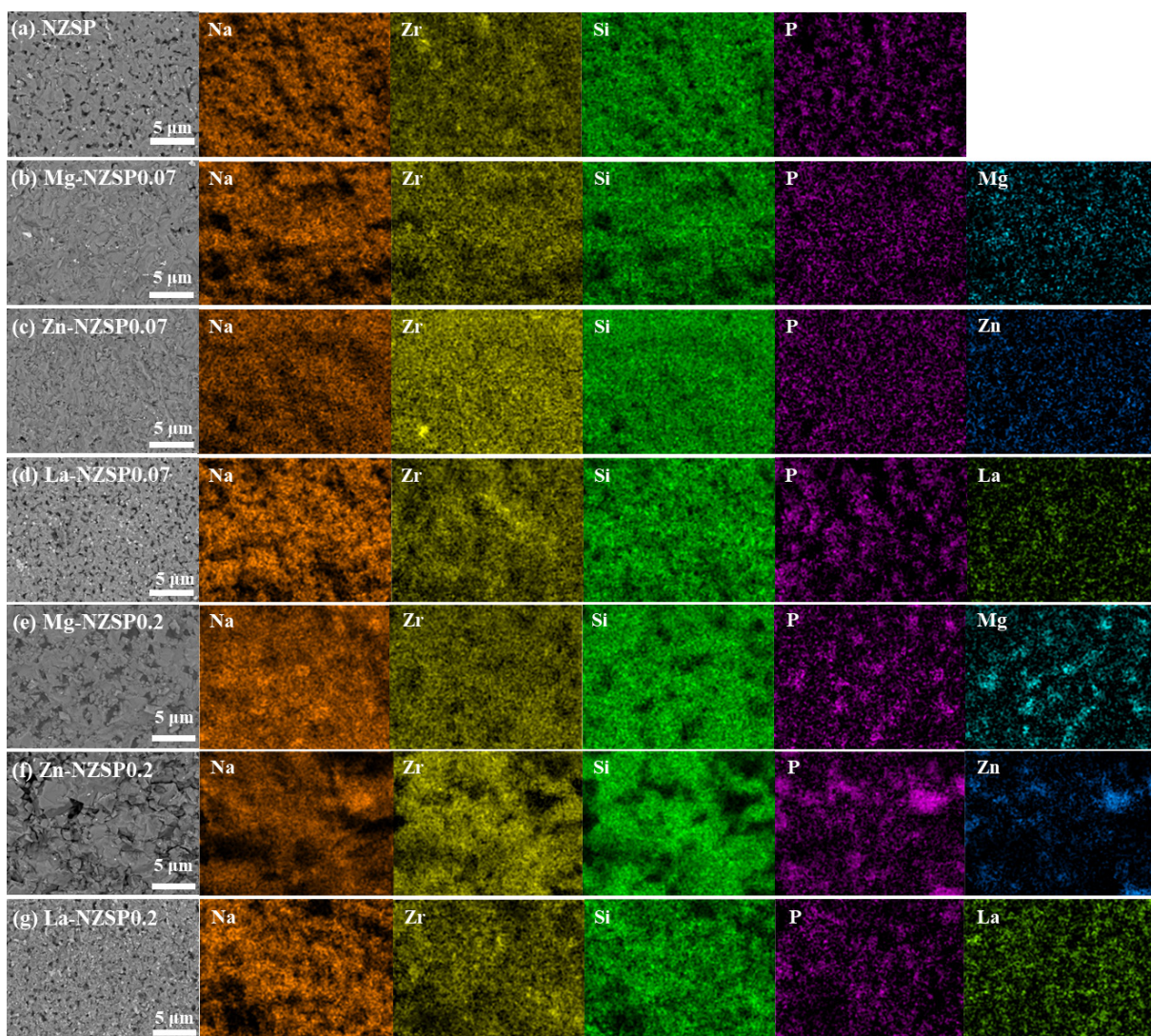


Fig. 4 EDS elemental mapping of NASICON ceramics: (a) NZSP, (b) Mg-NZSP0.07, (c) Zn-NZSP0.07, (d) La-NZSP0.07, (e) Mg-NZSP0.2, (f) Zn-NZSP0.2, and (g) La-NZSP0.2.

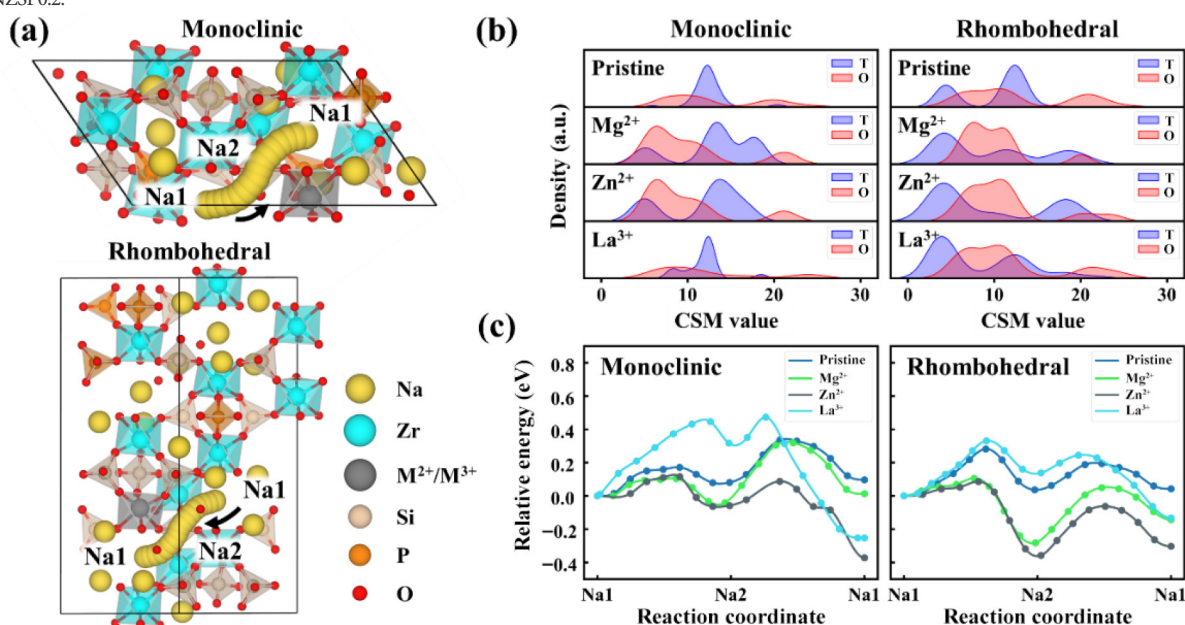


Fig. 5 (a) Three-dimensional percolating Na^+ transport pathways in monoclinic and rhombohedral NZSP. (b) Kernel density estimation of the CSM value for Na^+ polyhedra in the NZSP structure. “T” indicates a tetrahedron, and “O” indicates an octahedron. (c) Activation energy barriers along the $\text{Na}_1\text{-}\text{Na}_2\text{-}\text{Na}_1$ diffusion pathway in monoclinic and rhombohedral NZSP.

similar channel size distributions, where the Na1 site has a larger surrounding space than Na2 does. In contrast, Mg-NZSP and Zn-NZSP exhibited a smaller size difference between the two Na^+ sites. These differences in the Na^+ site geometry are consistent with the observation that undoped NZSP has a similar migration energy trend to that of La-NZSP, whereas Mg-NZSP has a migration energy barrier comparable to that of Zn-NZSP. As a result, in both crystal structures, doping with Mg^{2+} and Zn^{2+} are expected to positively influence Na-ion migration, whereas La^{3+} doping does not appear to provide such benefits.

Figure 6 displays the Nyquist plots, which include information on the bulk conductivity, grain boundary conductivity, and total conductivity of NASICON. The impedance spectrum of NASICON consists of a semicircle at high frequencies and a diagonal line at low frequencies. The point on the X-axis where the transition from high to low frequencies occurs represents the total resistance. The beginning of the semicircle indicates the bulk resistance, whereas the difference between the total resistance and the bulk resistance represents the grain boundary resistance. Undoped NZSP displays a large semicircle in the high-frequency spectrum, indicating high grain boundary resistance due to the numerous pores observed in the microstructure. As observed in the Nyquist plots for Mg^{2+} and Zn^{2+} , introducing an optimal amount of dopant reduces both the bulk and grain boundary resistances. The reduction in bulk resistance is attributed primarily

to the incorporation of dopants into the NASICON structure, which induces a phase transition to a more symmetric rhombohedral phase, thereby shortening the Na^+ migration pathways. Additionally, the increased Na^+ carrier concentration, introduced to maintain charge neutrality upon heteroatom doping, further contributes to this enhancement [83]. In particular, the diameter of the semicircle in the Nyquist plot, which corresponds to the grain boundary resistance, significantly decreased with the introduction of optimal Mg^{2+} and Zn^{2+} dopants. As discussed in the analysis of cross-sectional images of NASICON, the addition of these dopants promoted densification and accelerated grain growth, minimizing pore formation and resulting in a more compact microstructure. This change in microstructure directly reduced the grain boundary resistance of NASICON. The ionic conductivity and density of NASICON doped with heteroatoms are summarized in **Table 2**. NASICON doped with Mg^{2+} and Zn^{2+} demonstrated an increase in both the density and ionic conductivity up to a doping concentration of 0.07. Notably, Zn-NZSP0.07 has an ionic conductivity of $2.74 \times 10^{-3} \text{ S}\cdot\text{cm}^{-1}$, which is approximately 4.5-fold greater than that of the undoped NZSP ($6.00 \times 10^{-4} \text{ S}\cdot\text{cm}^{-1}$). Additionally, it achieves a high density of $3.24 \text{ g}\cdot\text{cm}^{-3}$, corresponding to a relative density of ~99.1% when considering the theoretical density of NASICON ($3.27 \text{ g}\cdot\text{cm}^{-3}$). However, for both dopants, NZSP with dopant ratios exceeding 0.1 exhibited a decrease in the main properties of

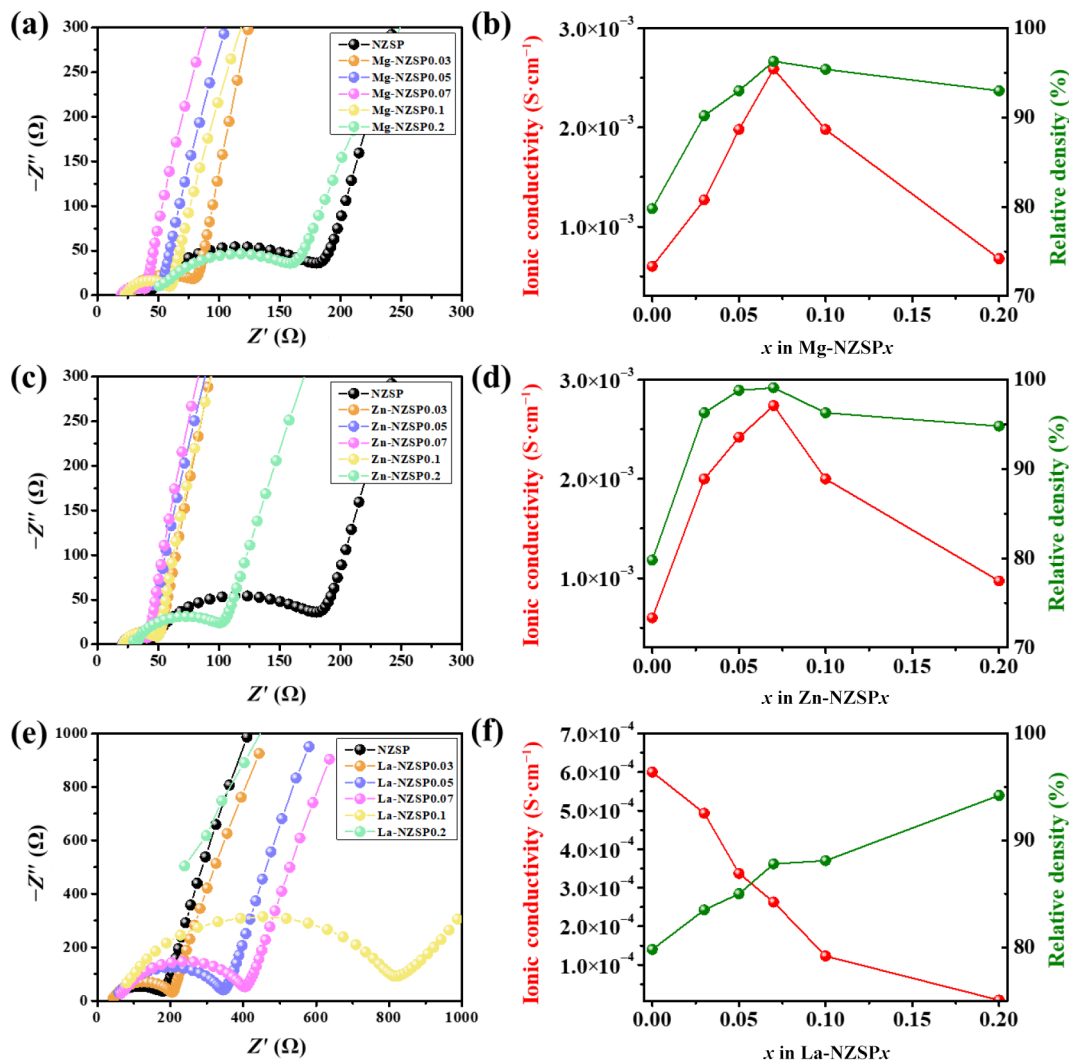


Fig. 6 Nyquist plots of the impedances, ionic conductivities, and relative densities for (a, b) Mg-NZSP x , (c, d) Zn-NZSP x , and (e, f) La-NZSP x .

the materials. This decrease can be attributed to the formation of secondary phases resulting from the interaction of Na and P with the dopants rather than their substitution within the crystal structure, which adversely affects the properties of the materials. Additionally, NZSP doped with La³⁺ demonstrates reduced ionic conductivity even at low doping levels, likely due to the inability of La³⁺ to incorporate into the crystal structure during the synthesis process. Furthermore, even if La³⁺ is incorporated into the NASICON structure, it has a lesser effect on channel distortion than Mg²⁺ or Zn²⁺ does, making it less effective in promoting ionic conductivity. Based on these findings, La³⁺ was deemed unsuitable

as a candidate under the current experimental conditions. Consequently, we excluded La³⁺ from further electrochemical analyses and conducted a more detailed investigation into the Mg²⁺ and Zn²⁺ dopants.

The activation energy (E_a) was calculated via an Arrhenius plot in the temperature range of 293–353 K (Fig. 7). All the samples exhibited a linear relationship between $1/T$ and $\log\sigma$, which is the characteristic of typical inorganic conductors. The calculated E_a values are 0.196 eV for Zn-NZSP0.07, 0.209 eV for Mg-NZSP0.07, and 0.243 eV for undoped NZSP. The optimized incorporation of heteroatoms induced a partial phase transition to a rhombohedral

Table 2 Bulk conductivity (σ_b), grain boundary conductivity (σ_{gb}), total conductivity (σ_t), density (g·cm⁻³), and relative density (%) of NASICON ceramics at room temperature

Composition	σ_b (S·cm ⁻¹)	σ_{gb} (S·cm ⁻¹)	σ_t (S·cm ⁻¹)	Density (g·cm ⁻³)	Relative density (%)
NZSP	2.28×10^{-3}	8.14×10^{-4}	6.00×10^{-4}	2.61	79.8
Mg-NZSP0.03	3.60×10^{-3}	1.95×10^{-3}	1.27×10^{-3}	2.95	90.2
Mg-NZSP0.05	3.99×10^{-3}	3.94×10^{-3}	1.98×10^{-3}	3.04	93.0
Mg-NZSP0.07	4.74×10^{-3}	5.69×10^{-3}	2.59×10^{-3}	3.15	96.3
Mg-NZSP0.1	4.64×10^{-3}	3.45×10^{-3}	1.98×10^{-3}	3.12	95.4
Mg-NZSP0.2	2.06×10^{-3}	1.01×10^{-3}	6.77×10^{-4}	3.04	93.0
Zn-NZSP0.03	4.25×10^{-3}	3.76×10^{-3}	2.00×10^{-3}	3.15	96.3
Zn-NZSP0.05	4.64×10^{-3}	5.04×10^{-3}	2.42×10^{-3}	3.23	98.8
Zn-NZSP0.07	4.76×10^{-3}	6.45×10^{-3}	2.74×10^{-3}	3.24	99.1
Zn-NZSP0.1	4.26×10^{-3}	3.78×10^{-3}	2.00×10^{-3}	3.15	96.3
Zn-NZSP0.2	2.95×10^{-3}	1.45×10^{-3}	9.72×10^{-4}	3.10	94.8
La-NZSP0.03	2.15×10^{-3}	6.40×10^{-4}	4.93×10^{-4}	2.73	83.5
La-NZSP0.05	2.05×10^{-3}	4.04×10^{-4}	3.37×10^{-4}	2.78	85.0
La-NZSP0.07	1.68×10^{-3}	3.11×10^{-4}	2.63×10^{-4}	2.94	89.9
La-NZSP0.1	1.22×10^{-3}	1.36×10^{-4}	1.23×10^{-4}	2.88	88.1
La-NZSP0.2	4.38×10^{-4}	8.69×10^{-6}	8.52×10^{-6}	3.08	94.2

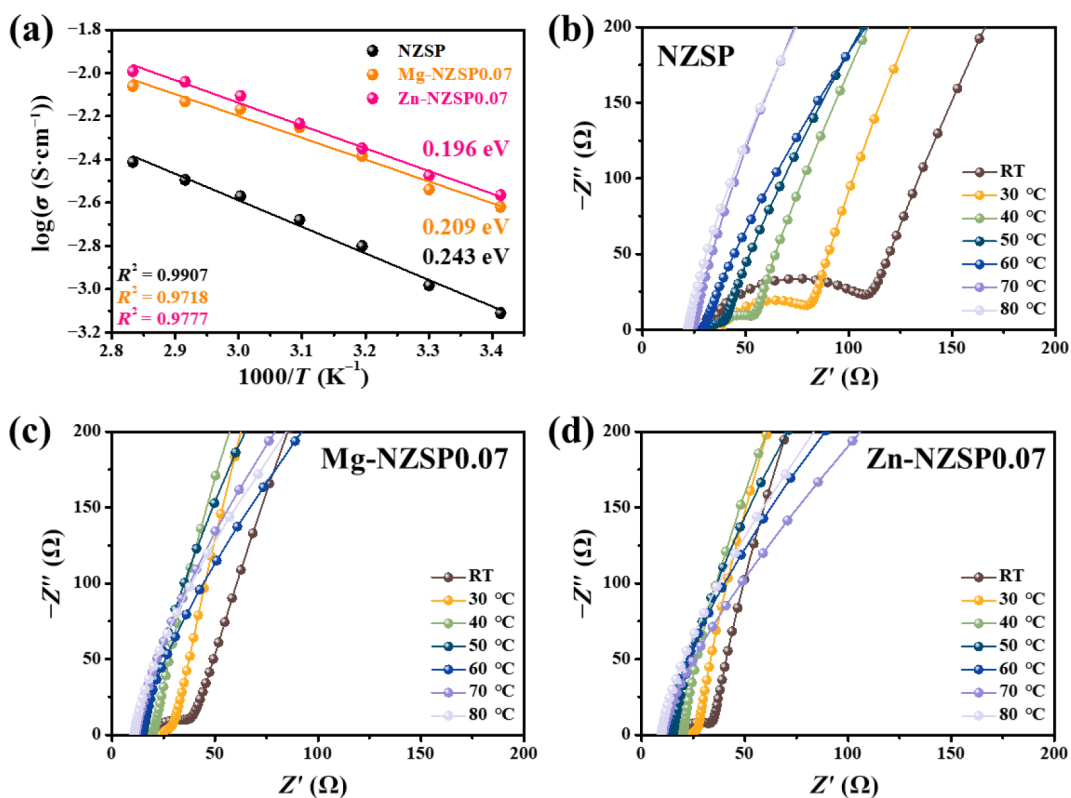


Fig. 7 (a) Arrhenius plots of undoped NZSP, Mg-NZSP0.07, and Zn-NZSP0.07. Nyquist plots of (b) undoped NZSP, (c) Mg-NZSP0.07, and (d) Zn-NZSP0.07 over the temperature range of 293–353 K.

structure, increased the concentration of sodium ions needed for charge balancing, and reduced the grain boundary resistance due to the denser microstructure. Consequently, the activation energies for sodium ion movement in Zn-NZSP0.07 and Mg-NZSP0.07 were significantly reduced, as shown in Fig. 7.

Additionally, the electronic conductivities of NZSP and their stability across a wide range of voltages were evaluated. The electronic conductivity was analyzed via the DC polarization method (Fig. S8(a) in the ESM). When a voltage of 6 V was applied, the current quickly converged to 0 A, indicating the low electronic conductivities of all the samples. The calculated electronic conductivities derived from the measured current values are 5.83×10^{-8} S·cm⁻¹ for undoped NZSP, 2.00×10^{-8} S·cm⁻¹ for Mg-NZSP0.07, and 7.07×10^{-9} S·cm⁻¹ for Zn-NZSP0.07. The lower the electronic conductivity and the higher the relative density of NASICON are, the more effectively the formation and growth of sodium dendrites are suppressed. This is crucial for improving the electrochemical properties of solid-electrolyte-based batteries. The low electronic conductivity of the solid electrolyte can help mitigate internal short circuits, thereby enhancing the safety of the battery. Cyclic voltammetry (CV) measurements were conducted via a Na||Zn-NZSP0.07||stainless steel cell in the voltage range from -1 to 5 V to investigate the electrochemical window of the optimal NASICON sample. Figure S8(b) in the ESM shows two oxidation and reduction peaks near 0 V, which are attributed to sodium metal plating and stripping. Apart from these peaks, no other current peaks were observed up to 5 V, indicating that the optimal NASICON electrolyte possesses a wide electrochemical window.

Figure 8 presents the results of the bending strength tests for NASICON. The mechanical strength of ceramic solid electrolytes is a critical performance factor closely linked to battery stability. During high-power operation or extended cycles, metal dendrites tend to form and grow irregularly with prolonged use, a phenomenon commonly observed in lithium- and sodium-based secondary batteries [72]. When these metal dendrites penetrate the electrolyte and contact the electrode, short circuits occur,

leading to battery failure. To suppress this issue, a ceramic electrolyte with high mechanical strength is needed, which can be achieved through improved densification [84]. Our previous experimental results confirmed the densification of NASICON through heteroatom doping. To evaluate the relationship between density and strength, we conducted three-point bending tests using a UTM system. The sample dimensions were standardized to a square with a side length of 3 cm and a thickness of 1 mm (Fig. 8(a)). The width of the bending jig was set to 20 mm, corresponding to two-thirds of the sample length, to ensure a uniform load distribution across all three points (Fig. 8(b)). The test results revealed that the baseline sample, undoped NZSP, had a strength of 29.74 MPa, whereas Mg-NZSP0.07 and Zn-NZSP0.07 had significantly higher strengths of 99.72 and 116.8 MPa, respectively. In contrast, La-NZSP0.07 exhibited a flexural strength of 43.61 MPa, indicating that the mechanical strength does not follow a simple proportional relationship with the relative density (Fig. 8(c)). The presence of impurity phases such as ZrO₂ and Na_xLa_y(PO₄)_z in La-NZSP0.07 has been identified as a key factor that negatively affects the mechanical integrity of NASICON-based solid electrolytes. These findings suggest that optimized heteroatom doping strategies that suppress impurity formation can increase the mechanical strength, thereby effectively inhibiting dendrite growth and improving the structural stability of solid-state batteries.

Figure 9(a) presents data on the interfacial resistance measured using a Na symmetric cell. To mitigate the excessive interfacial resistance caused by poor wettability and facilitate a comparative analysis of each NASICON, this study introduced a gold interlayer between the NASICON and sodium metal [85,86]. The Nyquist plots in Fig. 9(a) show two semicircles. The first semicircle represents the resistance of the NASICON electrolyte itself, and the second semicircle represents the interfacial resistance between NASICON and Na metal. The interfacial resistance of undoped NZSP was approximately 600 Ω, whereas Zn-NZSP0.07 exhibited an interfacial resistance of approximately 70 Ω, indicating a ninefold reduction. This reduction is attributed to the improved contact between the Na metal anode and the NASICON electrolyte due to the increased density of the optimal heteroatom-doped NASICON and the introduction of a thin Au interlayer [51,71].

To investigate the limits of sodium dendrite suppression in NASICON electrolytes, symmetric cells were tested at 60 °C to evaluate their critical current densities. The elevated temperature improved interfacial contact under identical pressure conditions by promoting deformation of the softened metal and the formation of a conformal interface, thereby enabling a clearer comparison of critical current densities among samples [87–88]. Figures 9(b)–9(d) show the symmetric cells tested with a gradually increasing current density ranging from 0.01 to 1.5 mA·cm⁻². The results indicate that the maximum current density for the Zn-NZSP0.07 symmetric cell was 1.4 mA·cm⁻², which was higher than the 0.6 mA·cm⁻² for the undoped NZSP symmetric cell. The symmetric cell using Mg-NZSP0.07 also showed an improved maximum current density of 1.1 mA·cm⁻². The long-term cycling performance of the symmetric cells showed similar trends to those observed in the critical current density tests. Initially, the current was applied at 0.1 mA·cm⁻², and the stability was monitored by increasing the current by 0.1 mA·cm⁻² after a certain period. The cycling test results indicate that the voltage increased sharply at 0.4 mA·cm⁻² for undoped NZSP (Fig. 9(e)), 0.5 mA·cm⁻² for Mg-NZSP0.07 (Fig. 9(f)), and 0.8 mA·cm⁻² for Zn-NZSP0.07 (Fig. 9(g)). The symmetric cell using Zn-NZSP0.07 provided stable cycling

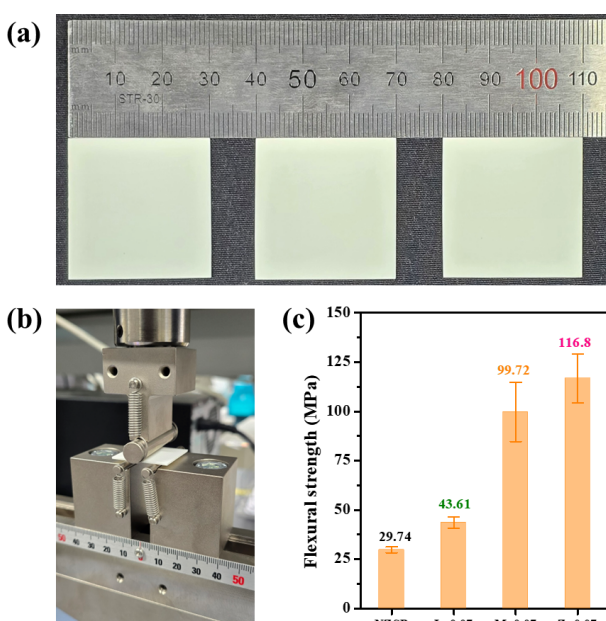


Fig. 8 Three-point bending strength tests of NASICON square pellets were performed via a universal testing machine (UTM). (a) Preparation of testing samples. (b) Bending test jig of the UTM. (c) Flexural strength test results of NZSP square-shaped pellets.

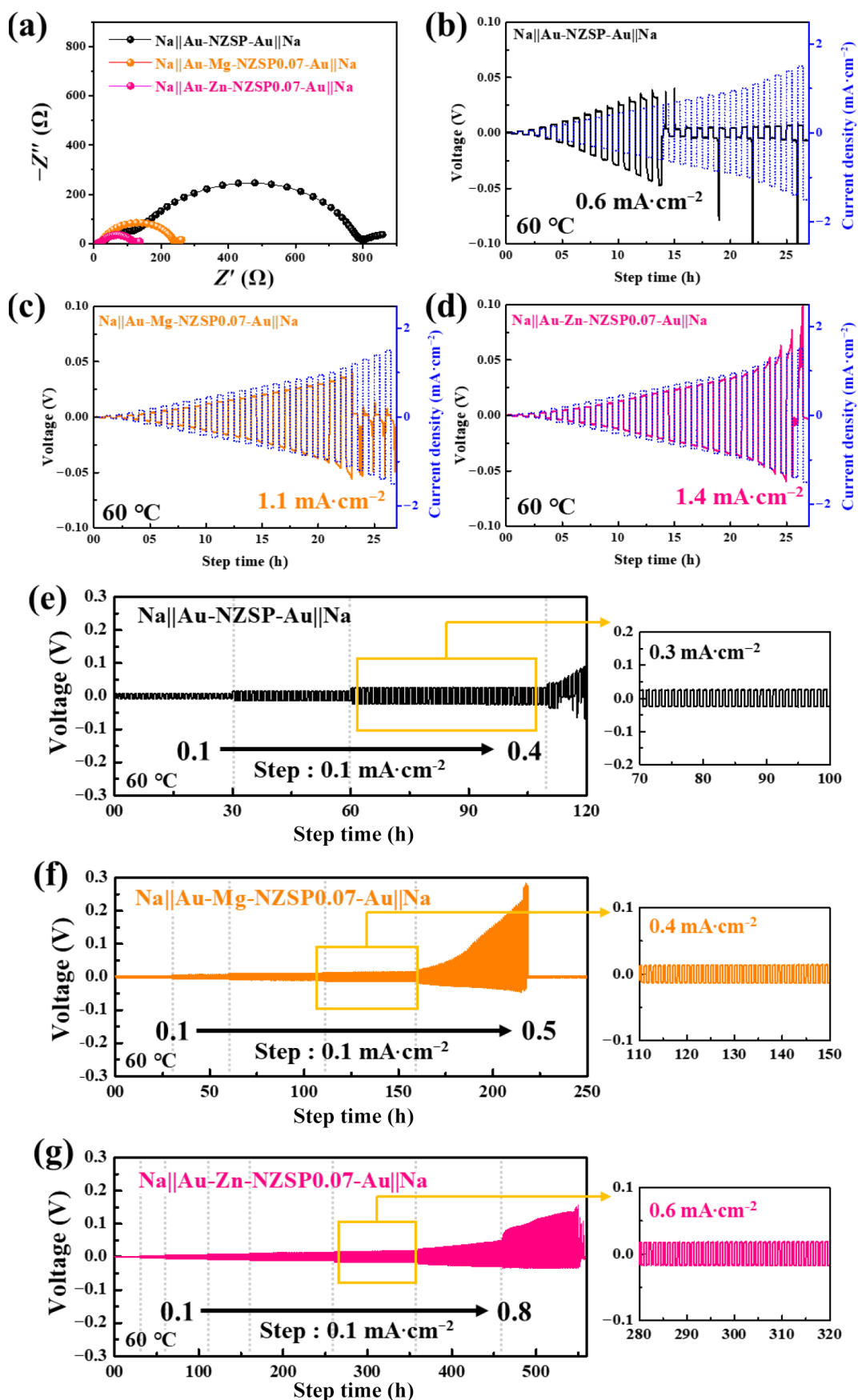


Fig. 9 (a) Nyquist plots for symmetric cells. Analysis of critical current density (CCD) using a symmetric cell measured at 60°C : (b) $\text{Na}||\text{Au-NZSP-Au}||\text{Na}$, (c) $\text{Na}||\text{Au-Mg-NZSP0.07-Au}||\text{Na}$, and (d) $\text{Na}||\text{Au-Zn-NZSP0.07-Au}||\text{Na}$. Galvanostatic cycling test of symmetric cells with increasing current density of $0.1 \text{ mA}\cdot\text{cm}^{-2}$: (e) $\text{Na}||\text{Au-NZSP-Au}||\text{Na}$, (f) $\text{Na}||\text{Au-Mg-NZSP0.07-Au}||\text{Na}$, and (g) $\text{Na}||\text{Au-Zn-NZSP0.07-Au}||\text{Na}$.

for over 500 h during the long-term current charge/discharge test. These results confirm that heteroatom doping enhances the densification of the ceramic electrolyte, thereby improving the mechanical strength and contributing to the suppression of sodium dendrite formation along the grain boundaries [69]. Compared with undoped NZSP, the optimized heteroatom-doped samples presented a higher critical current density and superior constant-current cycling stability, indicating significant improvements in the electrochemical performance [89].

To evaluate the electrochemical performance of solid-state sodium metal batteries, NVP||NASICON||Na cells were assembled with $\text{Na}_3\text{V}_2(\text{PO}_4)_3$ (NVP) as the cathode, sodium metal as the anode, and NASICON as the solid electrolyte. As shown in Fig. 10(a), the solid-state sodium cells with the Mg-NZSP0.07 and Zn-NZSP0.07 solid electrolytes demonstrated higher discharge capacities at elevated current densities than did the undoped NZSP. Specifically, the discharge capacities of Zn-NZSP0.07 were 109.6, 101.2, 96.4, 92.4, and 89.3 $\text{mAh}\cdot\text{g}^{-1}$ at 0.01, 0.05, 0.1, 0.15, and 0.2 $\text{A}\cdot\text{g}^{-1}$, respectively. Upon returning the current to 0.01 $\text{A}\cdot\text{g}^{-1}$, the cell retained a reversible capacity of 104.7 $\text{mAh}\cdot\text{g}^{-1}$. The charge/discharge voltage profiles at different current densities are presented in Fig. 10(b) and Fig. S9 in the ESM. The voltage profiles of the cells with NVP cathodes exhibit a charge/discharge plateau near ~3.4 V, corresponding to the insertion and extraction of Na^+ ions during the $\text{V}^{3+}/\text{V}^{4+}$ redox reaction [90]. As the current density increased from 0.01 to 0.2 $\text{A}\cdot\text{g}^{-1}$, the polarization of undoped NZSP increased from 39 to 629 mV, while it increased from 38 to 454 mV for Mg-NZSP0.07 and from 34 to 432 mV for Zn-NZSP0.07. In these solid-state sodium cells, the electrochemical performance was affected primarily by the material properties of NASICON. These results demonstrate that

optimizing heteroatom doping enhances the ionic conductivity of NASICON, which distinctly reduces voltage polarization by lowering the resistance to sodium ion transport.

While Mg-NZSP0.07 and Zn-NZSP0.07 showed similar properties in terms of rate performance, notable differences emerged during cycling tests conducted at a fixed current density of 0.1 $\text{A}\cdot\text{g}^{-1}$ (Fig. 10(c)). The NVP||Zn-NZSP0.07||Na cell exhibited an initial capacity of 103.9 $\text{mAh}\cdot\text{g}^{-1}$ and retained 76.3 $\text{mAh}\cdot\text{g}^{-1}$ after 200 cycles, corresponding to a capacity retention rate of 73.4% of the initial capacity. In contrast, the NVP||NZSP||Na cell demonstrated a rapid decline in capacity after 90 cycles. The NVP||Mg-NZSP0.07||Na cell exhibited behavior similar to that of the Zn-NZSP0.07 cell for up to 170 cycles but experienced a sharp decrease in capacity thereafter. This capacity degradation is attributed to the lower interfacial stability between the solid electrolyte and the electrode [91]. While the NVP||Zn-NZSP0.07||Na cell maintained stable voltage profiles over prolonged cycles, the NVP||Mg-NZSP0.07||Na cell exhibited a rapid increase in voltage polarization and a shortened voltage plateau (Fig. 10(d) and Fig. S10 in the ESM). This change in the voltage curve is believed to be influenced by the deterioration of the electrode–electrolyte interface rather than the degradation of the electrode itself [92,93]. This is further supported by the evaluation results shown in Fig. 9, which demonstrate the relatively good interface characteristics of Zn-NZSP in a symmetric cell. In conclusion, the results of various materials and electrochemical analyses demonstrate the feasibility of a solid-state sodium battery with improved properties, including enhanced capacity, improved voltage efficiency, and stable cycling performance, achieved through the optimal incorporation of heteroatoms in vA-NASICON.

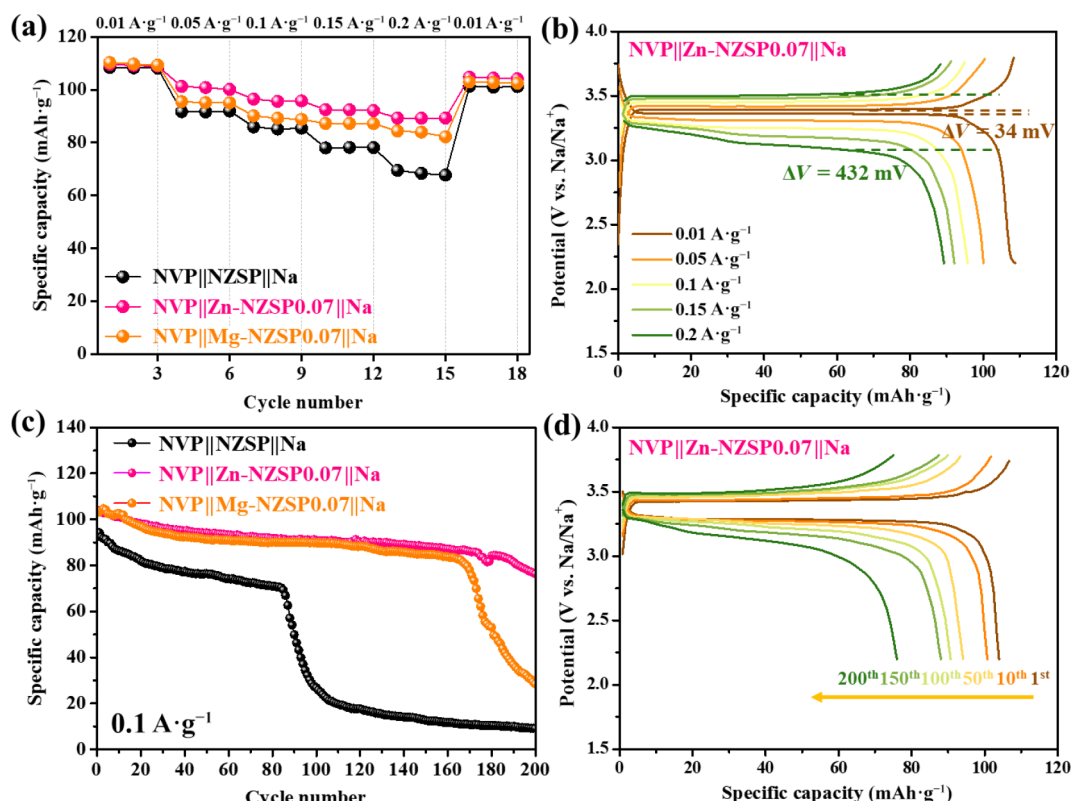


Fig. 10 (a) Rate properties of solid-state sodium cells of NVP||NZSP||Na, NVP||Zn-NZSP0.07||Na, and NVP||Mg-NZSP0.07||Na. (b) Voltage curves of NVP||Zn-NZSP0.07||Na cell operated under various current densities. (c) Cycling performance of solid-state sodium cells. (d) Voltage curves of NVP||Zn-NZSP0.07||Na cell operated at a current density of 0.1 $\text{A}\cdot\text{g}^{-1}$.

4 Conclusions

In this study, the applicability of heteroatom-doped vA-NASICON for solid-state sodium batteries was systematically evaluated. We investigated the aliovalent doping effects of three promising heteroatom candidates (Mg^{2+} , Zn^{2+} , and La^{3+}) that are expected to enhance the main properties of vA-NASICON. When optimal amounts of Mg^{2+} and Zn^{2+} were introduced, both the ionic conductivity and relative density increased, which was accompanied by the observation of a uniform NASICON crystalline phase. These experimental results were subsequently validated via computational methods. DFT, AIMD, and NEB simulations predicted that Zn^{2+} and Mg^{2+} would exhibit higher solubility limits than La^{3+} , thereby forming more stable NASICON phases. Moreover, the introduction of moderate structural distortion was found to facilitate Na^+ migration, leading to enhanced overall ionic conductivity. Among the synthesized samples, the optimal Zn^{2+} -doped vA-NASICON (Zn -NZSP0.07) exhibited the highest ionic conductivity and densification. Compared with undoped NASICON (NZSP), Zn -NZSP0.07 demonstrated a 4.5-fold increase in ionic conductivity, from 6.0×10^{-4} to $2.74 \times 10^{-3} \text{ S}\cdot\text{cm}^{-1}$, and a 24% increase in pellet density, from 2.61 to $3.24 \text{ g}\cdot\text{cm}^{-3}$. The average three-point bending strength was 116.8 MPa, which is four times greater than that of NZSP. In the symmetric critical current density cell test, Zn -NZSP0.07 endured a maximum current of $1.4 \text{ mA}\cdot\text{cm}^{-2}$. Additionally, it exhibited stable cycling performance for over 500 h in the galvanostatic lifespan test. Furthermore, a solid-state sodium battery with a $Na_3V_2(PO_4)_3$ cathode demonstrated improved rate properties and excellent cycle stability. This improvement was attributed to the increased density and conductivity of the electrolyte, which effectively suppressed the growth of sodium dendrites formed during the plating and stripping processes. This work achieved significantly improved ionic conductivity, density, and electrochemical performance under optimized sintering conditions of 1180°C for 12 h. These results demonstrate that optimized heteroatom doping in vA-NASICON serves as a promising strategy to increase the performance of solid-state sodium batteries, providing a pathway for the development of next-generation solid-state sodium batteries.

Acknowledgements

This work was supported by Korea Research Institute for defense Technology planning and advancement (KRIT) grant funded by the Korea government (Defense Acquisition Program Administration (DAPA)) (No. 21-107-D00-009, Design and development of core materials and unit cells for seawater secondary batteries, 2025).

Author contributions

Gunhee Park: writing – review & editing, writing – original draft, investigation, formal analysis, data curation, validation, methodology, conceptualization, and visualization. Dong Won Jeon: writing – review & editing, writing – original draft, investigation, methodology, and software. Il-Seop Jang: conceptualization, investigation, and methodology. Byeong-Jun Ahn: resources and validation. Kisang Baek: resources and validation. Bo-Ye Song: validation. Eun-hye Kim: investigation. Junho Bang: resources. Yun Chan Kang: writing – review & editing, writing – original draft, conceptualization, and supervision. Sung Beom Cho: writing – review & editing, writing – original draft, conceptualization, and supervision. Jinyoung Chun: writing – review & editing, writing – original draft, supervision, project administration, and conceptualization.

Availability of data and materials

The data that support the findings of this study are available from the corresponding author upon reasonable request.

Competing interests

The authors have no competing interests to declare that are relevant to the content of this article.

Electronic Supplementary Material

Supplementary material is available in the online version of this article at <https://doi.org/10.26599/JAC.2025.9221138>.

References

- [1] Li Y, Li M, Sun Z, et al. Recent advance on NASICON electrolyte in solid-state sodium metal batteries. *Energy Storage Mater* 2023, **56**: 582–599.
- [2] Goodenough JB. Energy storage materials: A perspective. *Energy Storage Mater* 2015, **1**: 158–161.
- [3] Feng XN, Ouyang MG, Liu X, et al. Thermal runaway mechanism of lithium ion battery for electric vehicles: A review. *Energy Storage Mater* 2018, **10**: 246–267.
- [4] Palomares V, Serras P, Villaluenga I, et al. Na-ion batteries, recent advances and present challenges to become low cost energy storage systems. *Energy Environ Sci* 2012, **5**: 5884–5901.
- [5] Pan HL, Hu YS, Chen LQ. Room-temperature stationary sodium-ion batteries for large-scale electric energy storage. *Energy Environ Sci* 2013, **6**: 2338–2360.
- [6] Wang QD, Zhou D, Zhao CL, et al. Fast-charge high-voltage layered cathodes for sodium-ion batteries. *Nat Sustain* 2024, **7**: 338–347.
- [7] Hu DN, Huang S, Wen Z, et al. A review on thermal runaway warning technology for lithium-ion batteries. *Renew Sustain Energy Rev* 2024, **206**: 114882.
- [8] Zheng Q, Yi HM, Li XF, et al. Progress and prospect for NASICON-type $Na_3V_2(PO_4)_3$ for electrochemical energy storage. *J Energy Chem* 2018, **27**: 1597–1617.
- [9] Wang H, Zhao GF, Wang SM, et al. Enhanced ionic conductivity of a $Na_3Zr_2Si_2PO_{12}$ solid electrolyte with Na_2SiO_3 obtained by liquid phase sintering for solid-state Na^+ batteries. *Nanoscale* 2022, **14**: 823–832.
- [10] Lee B, Paek E, Mitlin D, et al. Sodium metal anodes: Emerging solutions to dendrite growth. *Chem Rev* 2019, **119**: 5416–5460.
- [11] Slater MD, Kim D, Lee E, et al. Sodium-ion batteries. *Adv Funct Mater* 2013, **23**: 947–958.
- [12] Goodenough JB. Rechargeable batteries: Challenges old and new. *J Solid State Electrochem* 2012, **16**: 2019–2029.
- [13] Zhou CT, Bag S, Thangadurai V. Engineering materials for progressive all-solid-state Na batteries. *ACS Energy Lett* 2018, **3**: 2181–2198.
- [14] Zhao CL, Liu LL, Qi XG, et al. Solid-state sodium batteries. *Adv Energy Mater* 2018, **8**: 1703012.
- [15] Liu GZ, Sun XR, Yu XQ, et al. $Na_{10}SnSb_2S_{12}$: A nanosized air-stable solid electrolyte for all-solid-state sodium batteries. *Chem Eng J* 2021, **420**: 127692.
- [16] Hwang JY, Myung ST, Sun YK. Sodium-ion batteries: Present and future. *Chem Soc Rev* 2017, **46**: 3529–3614.
- [17] Lu Y, Li L, Zhang Q, et al. Electrolyte and interface engineering for solid-state sodium batteries. *Joule* 2018, **2**: 1747–1770.
- [18] Gamo H, Phuc NHH, Matsuda R, et al. Multiphase Na_3SbS_4 with high ionic conductivity. *Mater Today Energy* 2019, **13**: 45–49.
- [19] Jian ZL, Hu YS, Ji XL, et al. NASICON-structured materials for energy storage. *Adv Mater* 2017, **29**: 1601925.
- [20] Hou WR, Guo XW, Shen XY, et al. Solid electrolytes and interfaces in all-solid-state sodium batteries: Progress and perspective. *Nano Energy* 2018, **52**: 279–291.
- [21] Noguchi Y, Kobayashi E, Plashnitsa LS, et al. Fabrication and

- performances of all solid-state symmetric sodium battery based on NASICON-related compounds. *Electrochim Acta* 2013, **101**: 59–65.
- [22] Lalère F, Leriche JB, Courty M, et al. An all-solid state NASICON sodium battery operating at 200 °C. *J Power Sources* 2014, **247**: 975–980.
- [23] Tanibata N, Matsuyama T, Hayashi A, et al. All-solid-state sodium batteries using amorphous TiS₃ electrode with high capacity. *J Power Sources* 2015, **275**: 284–287.
- [24] Hayashi A, Noi K, Sakuda A, et al. Superionic glass-ceramic electrolytes for room-temperature rechargeable sodium batteries. *Nat Commun* 2012, **3**: 856.
- [25] Li MY, Dixit M, Essehli R, et al. Na₃Zr₂Si₂PO₁₂ solid electrolyte membrane for high-performance seawater battery. *Adv Sci* 2023, **10**: 2300920.
- [26] Go W, Kim J, Pyo J, et al. Investigation on the structure and properties of Na_{3.1}Zr_{1.55}Si_{2.3}P_{0.7}O₁₁ as a solid electrolyte and its application in a seawater battery. *ACS Appl Mater Inter* 2021, **13**: 52727–52735.
- [27] Goodenough JB, Hong HY, Kafalas JA. Fast Na⁺-ion transport in skeleton structures. *Mater Res Bull* 1976, **11**: 203–220.
- [28] Hong HY. Crystal structures and crystal chemistry in the system Na_{1+x}Zr_xSi_{3-x}O₁₂. *Mater Res Bull* 1976, **11**: 173–182.
- [29] Oh JAS, He LC, Plewa A, et al. Composite NASICON (Na₃Zr₂Si₂PO₁₂) solid-state electrolyte with enhanced Na⁺ ionic conductivity: Effect of liquid phase sintering. *ACS Appl Mater Inter* 2019, **11**: 40125–40133.
- [30] Zhang ZZ, Wenzel S, Zhu YZ, et al. Na₃Zr₂Si₂PO₁₂: A stable Na⁺-ion solid electrolyte for solid-state batteries. *ACS Appl Energy Mater* 2020, **3**: 7427–7437.
- [31] Ruan YL, Guo F, Liu JJ, et al. Optimization of Na₃Zr₂Si₂PO₁₂ ceramic electrolyte and interface for high performance solid-state sodium battery. *Ceram Int* 2019, **45**: 1770–1776.
- [32] Niu W, Chen L, Liu YC, et al. All-solid-state sodium batteries enabled by flexible composite electrolytes and plastic-crystal interphase. *Chem Eng J* 2020, **384**: 123233.
- [33] Noi K, Suzuki K, Tanibata N, et al. Liquid-phase sintering of highly Na⁺ ion conducting Na₃Zr₂Si₂PO₁₂ ceramics using Na₃BO₃ additive. *J Am Ceram Soc* 2018, **101**: 1255–1265.
- [34] Wi TU, Lee C, Rahman MF, et al. Chemical stability and degradation mechanism of solid electrolytes/aqueous media at a steady state for long-lasting sodium batteries. *Chem Mater* 2021, **33**: 126–135.
- [35] McEntire BJ, Bartlett RA, Miller GR, et al. Effect of decomposition on the densification and properties of nasicon ceramic electrolytes. *J Am Ceram Soc* 1983, **66**: 738–742.
- [36] Von Alpen U, Bell MF, Höfer HH. Compositional dependence of the electrochemical and structural parameters in the Nasicon system (Na_{1+x}Si_xZr₂P_{3-x}O₁₂). *Solid State Ion* 1981, **3**: 215–218.
- [37] Kuriakose AK, Wheat TA, Ahmad A, et al. Synthesis, sintering, and microstructure of NASICONs. *J Am Ceram Soc* 1984, **67**: 179–183.
- [38] Kohler H, Schulz H, Melnikov O. Composition and conduction mechanism of the NASICON structure X-ray diffraction study on two crystals at different temperatures. *Mater Res Bull* 1983, **18**: 1143–1152.
- [39] Oh JAS, Sun JG, Goh M, et al. A robust solid–solid interface using sodium–tin alloy modified metallic sodium anode paving way for all-solid-state battery. *Adv Energy Mater* 2021, **11**: 2101228.
- [40] Wang XX, Chen JJ, Wang DJ, et al. Improving the alkali metal electrode/inorganic solid electrolyte contact via room-temperature ultrasound solid welding. *Nat Commun* 2021, **12**: 7109.
- [41] Jolley AG, Cohn G, Hitz GT, et al. Improving the ionic conductivity of NASICON through aliovalent cation substitution of Na₃Zr₂Si₂PO₁₂. *Ionics* 2015, **21**: 3031–3038.
- [42] Zhang YY, Gao TY, Yu JM, et al. Mn dopant Na₃Zr₂Si₂PO₁₂ with enhanced ionic conductivity for quasi-solid-state sodium-metal battery. *ACS Appl Mater Inter* 2025, **17**: 10722–10731.
- [43] He JX, Yang SS, Xiao X, et al. Aliovalent cation substitution in Na₃Zr₂Si₂PO₁₂ for practical solid-state sodium metal batteries. *Energy Storage Mater* 2025, **75**: 104037.
- [44] Ma Q, Guin M, Naqash S, et al. Scandium-substituted Na₃Zr₂(SiO₄)₂ (PO₄) prepared by a solution-assisted solid-state reaction method as sodium-ion conductors. *Chem Mater* 2017, **28**: 4821–4828.
- [45] Liu SY, Zhou C, Wang Y, et al. Ce-substituted nanograin Na₃Zr₂Si₂PO₁₂ prepared by LF-FSP as sodium-ion conductors. *ACS Appl Mater Inter* 2020, **12**: 3502–3509.
- [46] Zou ZY, Ma N, Wang AP, et al. Identifying migration channels and bottlenecks in monoclinic NASICON-type solid electrolytes with hierarchical ion-transport algorithms. *Adv Funct Mater* 2021, **31**: 2107747.
- [47] Wang CZ, Sun Z, Zhao YJ, et al. Grain boundary design of solid electrolyte actualizing stable all-solid-state sodium batteries. *Small* 2021, **17**: 2103819.
- [48] Zhang LX, Liu YM, Han J, et al. Al doped into Si/P sites of Na₃Zr₂Si₂PO₁₂ with conducted Na₃PO₄ impurities for enhanced ionic conductivity. *ACS Appl Mater Inter* 2023, **15**: 44867–44875.
- [49] Jung SW, Wang JE, Kim DG, et al. Rare-earth element substitution of Na_{1+x}Zr₂Si_xP_{3-x}O₁₂ ($x = 2$) solid electrolyte: Implications for all-solid-state Na ion batteries. *ACS Appl Nano Mater* 2022, **5**: 13894–13902.
- [50] Ruan YL, Song SD, Liu JJ, et al. Improved structural stability and ionic conductivity of Na₃Zr₂Si₂PO₁₂ solid electrolyte by rare earth metal substitutions. *Ceram Int* 2017, **43**: 7810–7815.
- [51] Akbar M, Kim M, Moeez I, et al. Dendrite-free Sb-doped NASICON-type Na₃Zr₂Si₂PO₁₂ solid-electrolyte for stable solid-state sodium batteries. *Chem Eng J* 2025, **504**: 158860.
- [52] He DS, Xu PY, Ma DX, et al. Mg²⁺/F[−] synergy to enhance the ionic conductivity of Na₃Zr₂Si₂PO₁₂ solid electrolyte for solid-state sodium batteries. *ChemElectroChem* 2020, **7**: 2087–2094.
- [53] Luo J, Zhao GL, Qiang WJ, et al. Synthesis of Na ion-electron mixed conductor Na₃Zr₂Si₂PO₁₂ by doping with transition metal elements (Co, Fe, Ni). *J Am Ceram Soc* 2022, **105**: 3428–3437.
- [54] Wang WT, Yuan WY, Zhao ZJ, et al. Enhanced ionic conductivity of Cu-doped NASICON solid electrolyte for solid-state sodium batteries. *J Electroanal Chem* 2023, **937**: 117405.
- [55] Samiee M, Radhakrishnan B, Rice ZE, et al. Divalent-doped Na₃Zr₂Si₂PO₁₂ sodium superionic conductor: Improving the ionic conductivity via simultaneously optimizing the phase and chemistry of the primary and secondary phases. *J Power Sources* 2017, **347**: 229–237.
- [56] Sun F, Xiang YX, Sun Q, et al. Insight into ion diffusion dynamics/mechanisms and electronic structure of highly conductive sodium-rich Na_{3+x}La_xZr_{2-x}Si₂PO₁₂ ($0 \leq x \leq 0.5$) solid-state electrolytes. *ACS Appl Mater Inter* 2021, **13**: 13132–13138.
- [57] Kresse G, Furthmüller J. Efficient iterative schemes for *ab initio* total-energy calculations using a plane-wave basis set. *Phys Rev B* 1996, **54**: 11169–11186.
- [58] Blöchl PE. Projector augmented-wave method. *Phys Rev B* 1994, **50**: 17953–17979.
- [59] Perdew JP, Burke K, Ernzerhof M. Generalized gradient approximation made simple. *Phys Rev Lett* 1996, **77**: 3865–3868.
- [60] van de Walle A, Asta M, Ceder G. The alloy theoretic automated toolkit: A user guide. *Calphad* 2002, **26**: 539–553.
- [61] Jun K, Sun YZ, Xiao YH, et al. Lithium superionic conductors with corner-sharing frameworks. *Nat Mater* 2022, **21**: 924–931.
- [62] Evans DJ, Holian BL. The nose-hoover thermostat. *J Chem Phys* 1985, **83**: 4069–4074.
- [63] Ong SP, Richards WD, Jain A, et al. Python materials genomics (pymatgen): A robust, open-source Python library for materials analysis. *Comput Mater Sci* 2013, **68**: 314–319.
- [64] Willemets TF, Rycroft CH, Kazi M, et al. Algorithms and tools for high-throughput geometry-based analysis of crystalline porous materials. *Micropor Mesopor Mater* 2012, **149**: 134–141.
- [65] Momma K, Izumi F. VESTA 3 for three-dimensional visualization of crystal, volumetric and morphology data. *J Appl Crystallogr* 2011, **44**: 1272–1276.
- [66] Song SF, Duong HM, Korsunsky AM, et al. A Na⁺ superionic conductor for room-temperature sodium batteries. *Sci Rep* 2016, **6**: 32330.

- [67] Zhang ZZ, Zhang QH, Shi JN, et al. A self-forming composite electrolyte for solid-state sodium battery with ultralong cycle life. *Adv Energy Mater* 2017, **7**: 1601196.
- [68] Chen CY, et al. The impact of La doping on the ionic conductivity of $\text{Na}_{3+x}\text{La}_x\text{Zr}_{2-x}\text{Si}_2\text{PO}_{12}$ solid-state electrolytes. *J Phys Chem C* 2025, **129**: 3414–3423.
- [69] Lu Y, Alonso JA, Yi Q, et al. A high-performance monolithic solid-state sodium battery with Ca^{2+} doped $\text{Na}_3\text{Zr}_2\text{Si}_2\text{PO}_{12}$ electrolyte. *Adv Energy Mater* 2019, **9**: 1901205.
- [70] Wang JH, Kang JR, Guo X, et al. Enhanced ionic conductivity in $\text{Na}_3\text{Zr}_2\text{Si}_2\text{PO}_{12}$ NASICON-type solid electrolytes by adding Mg^{2+} ions. *J Alloys Compd* 2024, **988**: 174327.
- [71] Yang L, Wang H, Liu Q, et al. Increase ionic conductivity of a $\text{Zn}^{2+}/\text{F}^-$ synergy $\text{Na}_3\text{Zr}_2\text{Si}_2\text{PO}_{12}$ solid electrolyte for sodium metal batteries. *J Eur Ceram Soc* 2023, **43**: 4443–4450.
- [72] Shen L, Yang J, Liu G, et al. High ionic conductivity and dendrite-resistant NASICON solid electrolyte for all-solid-state sodium batteries. *Mater Today Energy* 2021, **20**: 100691.
- [73] Jang IS, Go W, Song BY, et al. Improving ionic conductivity of von-Alpen-type NASICON ceramic electrolytes via magnesium doping. *J Adv Ceram* 2023, **12**: 1058–1066.
- [74] Thirupathi R, Omar S. A strategic co-doping approach using Sc^{3+} and Ce^{4+} toward enhanced conductivity in NASICON-type $\text{Na}_3\text{Zr}_2\text{Si}_2\text{PO}_{12}$. *J Phys Chem C* 2021, **125**: 27723–27735.
- [75] Shindrov AA. Increasing sinterability and ionic conductivity of $\text{Na}_3\text{Zr}_2\text{Si}_2\text{PO}_{12}$ ceramics by high energy ball-milling. *Solid State Ion* 2023, **391**: 116139.
- [76] Berry KA, Harmer MP. Effect of MgO solute on microstructure development in Al_2O_3 . *J Am Ceram Soc* 1986, **69**: 143–149.
- [77] Cha JM, Liu LY, Lee HJ, et al. Crystallization kinetics of lithium–aluminum–germanium–phosphate glass doped with MgO using a non-isothermal method. *J Korean Ceram Soc* 2021, **58**: 614–622.
- [78] Yang J, Liu GZ, Avdeev M, et al. Ultrastable all-solid-state sodium rechargeable batteries. *ACS Energy Lett* 2020, **5**: 2835–2841.
- [79] Tseng CF, Chen PH, Lin PA. Low temperature sintering and microwave dielectric properties of $\text{Zn}_{0.5}\text{Ti}_{0.5}\text{NbO}_4$ ceramics with ZnO additive for LTCC applications. *J Alloys Compd* 2015, **632**: 810–815.
- [80] Di Stefano D, Miglio A, Robeys K, et al. Superionic diffusion through frustrated energy landscape. *Chem* 2019, **5**: 2450–2460.
- [81] Wang Y, Richards WD, Ong SP, et al. Design principles for solid-state lithium superionic conductors. *Nat Mater* 2015, **14**: 1026–1031.
- [82] Henkelman G, Uberuaga BP, Jónsson H. A climbing image nudged elastic band method for finding saddle points and minimum energy paths. *J Chem Phys* 2000, **113**: 9901–9904.
- [83] Jolley AG, Taylor DD, Schreiber NJ, et al. Structural investigation of monoclinic-rhombohedral phase transition in $\text{Na}_3\text{Zr}_2\text{Si}_2\text{PO}_{12}$ and doped NASICON. *J Am Ceram Soc* 2015, **98**: 2902–2907.
- [84] Liu GZ, Weng W, Zhang ZH, et al. Densified $\text{Li}_6\text{PS}_5\text{Cl}$ nanorods with high ionic conductivity and improved critical current density for all-solid-state lithium batteries. *Nano Lett* 2020, **20**: 6660–6665.
- [85] Zhou WD, Li YT, Xin S, et al. Rechargeable sodium all-solid-state battery. *ACS Cent Sci* 2017, **3**: 52–57.
- [86] Sampathkumar R, Echeverría M, Zhang Y, et al. Interface stability between $\text{Na}_3\text{Zr}_2\text{Si}_2\text{PO}_{12}$ solid electrolyte and sodium metal anode for quasi-solid-state sodium battery. *Batteries* 2023, **9**: 8.
- [87] Lu Y, Zhao CZ, Yuan H, et al. Critical current density in solid-state lithium metal batteries: Mechanism, influences, and strategies. *Adv Funct Mater* 2021, **31**: 2009925.
- [88] Huang X, Lu Y, Niu YJ, et al. From protonation & Li-rich contamination to grain-boundary segregation: Evaluations of solvent-free vs. wet routes on preparing $\text{Li}_7\text{La}_3\text{Zr}_2\text{O}_{12}$ solid electrolyte. *J Energy Chem* 2022, **73**: 223–239.
- [89] Tang XJ, Han WB, Zhang Y, et al. Interface engineering of sodium metal anode for all-solid-state sodium batteries. *J Power Sources* 2024, **623**: 235397.
- [90] Ra Y, Kim JH, Jung DS, et al. Structural optimization of NVP/C composites by an advanced two-step spray technique for high energy density and long-life symmetric sodium-ion batteries. *Small* 2025, **21**: 2411515.
- [91] He LC, Oh JAS, Watarai K, et al. Electromechanical failure of NASICON-type solid-state electrolyte-based all-solid-state Li-ion batteries. *Chem Mater* 2021, **33**: 6841–6852.
- [92] Ran LB, Baktash A, Li M, et al. Sc, Ge co-doping NASICON boosts solid-state sodium ion batteries' performance. *Energy Storage Mater* 2021, **40**: 282–291.
- [93] Tian HQ, Liu S, Deng LJ, et al. New-type Hf-based NASICON electrolyte for solid-state Na-ion batteries with superior long-cycling stability and rate capability. *Energy Storage Mater* 2021, **39**: 232–238.